# NEW INSIGHTS IN THE HII REGION G18.88−0.49: HUB-FILAMENT SYSTEM AND ACCRETING FILAMENTS

L. K. Dewangan[1], D. K. Ojha[2], Saurabh Sharma[3], S. del Palacio[4], N. K. Bhadari[1,5], and A. Das[6]

## ABSTRACT

We present an analysis of multi-wavelength observations of an area of $0°.27 \times 0°.27$ around the Galactic H II region G18.88−0.49, which is powered by an O-type star (age $\sim 10^5$ years). The *Herschel* column density map reveals a shell-like feature of extension $\sim 12$ pc $\times$ 7 pc and mass $\sim 2.9 \times 10^4$ $M_\odot$ around the H II region; its existence is further confirmed by the distribution of molecular ($^{12}$CO, $^{13}$CO, C$^{18}$O, and NH$_3$) gas at [60, 70] km s$^{-1}$. Four subregions are studied toward this shell-like feature, and show a mass range of $\sim 0.8$–$10.5 \times 10^3$ $M_\odot$. These subregions associated with dense gas are dominated by non-thermal pressure and supersonic non-thermal motions. The shell-like feature is associated with the H II region, Class I protostars, and a massive protostar candidate, illustrating the ongoing early phases of star formation (including massive stars). The massive protostar is found toward the position of the 6.7 GHz methanol maser, and is associated with outflow activity. Five parsec-scale filaments are identified in the column density and molecular maps, and appear to be radially directed to the dense parts of the shell-like feature. This configuration is referred to as a "hub-filament" system. Significant velocity gradients (0.8–1.8 km s$^{-1}$ pc$^{-1}$) are observed along each filament, suggesting that the molecular gas flows towards the central hub along the filaments. Overall, our observational findings favor a global non-isotropic collapse scenario as discussed in Motte et al. (2018), which can explain the observed morphology and star formation in and around G18.88−0.49.

*Subject headings:* dust, extinction – HII regions – ISM: clouds – ISM: individual object (G18.88-0.49) – stars: formation – stars: pre-main sequence

## 1. INTRODUCTION

Understanding the formation process of massive OB-type stars ($\gtrsim 8$ $M_\odot$) is still far from complete (Zinnecker & Yorke 2007; Tan et al. 2014; Motte et al. 2018). Dust and molecular filaments are often associated with dense massive star-forming clumps, H II regions excited by massive stars, and young stellar clusters (e.g., Myers 2009; André et al. 2010; Schneider et al. 2012; Tigé et al. 2017; Motte et al. 2018; Treviño-Morales et al. 2019; Kumar et al. 2020). It is thought that massive stars and clusters of young stellar objects (YSOs) commonly form within parsec-scale massive clumps/clouds such as hub-filament systems (e.g., Monoceros R2; Treviño-Morales et al. 2019) and ridges (e.g., DR 21). Hub-filament systems are known as a junction of three or more filaments (e.g., Myers 2009). In general, in hub-filament systems, filaments are traced with high aspect ratio (length/diameter) and lower column densities ($\sim 10^{21}$ cm$^{-2}$) compared to a hub system that is identified with low aspect ratio and high column density ($\sim 10^{22}$ cm$^{-2}$; e.g., Myers 2009; Schneider et al. 2012).

lokeshd@prl.res.in
[1] Physical Research Laboratory, Navrangpura, Ahmedabad - 380 009, India.
[2] Department of Astronomy and Astrophysics, Tata Institute of Fundamental Research, Homi Bhabha Road, Mumbai - 400005, India.
[3] Aryabhatta Research Institute of Observational Sciences (ARIES), Manora Peak, Nainital, 263002, India.
[4] Instituto Argentino de Radioastronomía (CCT La Plata, CONICET; CICPBA; UNLP), C.C.5, (1894) Villa Elisa, Buenos Aires, Argentina.
[5] Indian Institute of Technology Gandhinagar Palaj, Gandhinagar, 382355, India.
[6] University of Hyderabad, Hyderabad - 500046, India.

In relation to hub-filament systems, Motte et al. (2018) discussed an evolutionary scheme for the birth of massive stars (i.e., a global non-isotropic collapse scenario; see also Tigé et al. 2017) that takes into account the flavours of the global hierarchical collapse and clump-feed accretion scenarios (see Vázquez-Semadeni et al. 2009, 2017; Smith et al. 2009). Central to such study is the identification of a hub-filament system containing the highest density regions, where several filaments converge. Such investigation requires the knowledge of molecular gas motion in the hub-filament system. In this paper, we aim to identify embedded filaments and to investigate their role in the formation of massive OB-type stars and YSOs in the site hosting an H II region G18.88−0.49 (Kerton et al. 2013) and an Extended Green Object (EGO; Cyganowski et al. 2008).

Following this section, an overview of G18.88−0.49 is presented in Section 2. Section 3 gives the information of the various data sets used in this paper. In Section 4, we present the outcomes concerning the physical environment and point-like sources toward G18.88−0.49. In Section 5, we discuss possible star formation processes in G18.88−0.49. Finally, the major findings are summarized in Section 6.

## 2. OVERVIEW OF G18.88−0.49

The selected H II region G18.88−0.49 is associated with the large, about 30 pc diameter, inner-Galaxy H II region W39 ($l = 18°.7$–$19°.3$) powered by a cluster of massive OB stars (Westerhout 1958; Kerton et al. 2013). Figure 1a displays a large-scale view of the complex W39 using the *Herschel* 70 $\mu$m continuum image overlaid with the 20 cm continuum emission contour from the Multi-Array Galactic Plane Imaging Survey (MAGPIS; Helfand

et al. 2006). This figure reveals a wide-open bubble and an extended H II region in the direction of W39 (radial velocity ($V_{lsr}$) range = (60, 70) km s$^{-1}$; distance ∼4.7 kpc; see Kerton et al. 2013). Kerton et al. (2013) found a local minimum in the radio emission that allowed them to propose the position of the exciting star(s) of the W39 H II region, which is indicated in Figure 1a (see also Li et al. 2019). Figure 1a shows the positions of 52 APEX Telescope Large Area Survey of the Galaxy (AT-LASGAL; Schuller et al. 2009) clumps at 870 $\mu$m from Urquhart et al. (2018). These clumps are traced in a $V_{lsr}$ range of ∼[59.5, 70] km s$^{-1}$ and a distance of ∼5.0 kpc (see Table 2 in Urquhart et al. 2018). The H II region G18.88−0.49 is located toward the periphery of W39.

The molecular cloud associated with the H II region G18.88−0.49 was reported by Anderson et al. (2009), and is referred to as C18.88−0.49 ($V_{lsr}$ ∼65.5 km s$^{-1}$; distance ∼4.7 kpc). Kerton et al. (2013) reported that the H II region G18.88−0.49 is excited by a young O-type star (age ∼$10^5$ years). Li et al. (2019) studied the physical environment of W39 (including G18.88−0.49) using *Herschel* continuum images at 70–500 $\mu$m and the NH$_3$ line data. To examine the near-infrared and mid-infrared (MIR) view, Figure 1b shows a three color-composite image of G18.88−0.49 with *Spitzer* 24 $\mu$m in red, 8.0 $\mu$m in green, and 3.6 $\mu$m in blue (see a dotted-dashed box in Figure 1a). At least two MIR bubbles are seen in the *Spitzer* images, namely MWP-1G018879-004949 (radius = 1′.53) and MWP-1G018848-004761 (radius = 0′.88) (see arrows and dashed circles in Figure 1b), which were previously reported in the Milky Way Project bubbles catalog (Simpson et al. 2012). In Figure 1b, the positions of the radio recombination line (RRL) observations are marked (taken from Lockman 1989; Anderson et al. 2011). Apart from our selected target H II region, there is also another H II region, G18.937−0.434, labeled in Figure 1b. The H II regions G18.88−0.49 and G18.937−0.434 are depicted in the ionized gas velocity of 65.5 and 68 km s$^{-1}$, respectively (e.g., Lockman 1989; Anderson et al. 2011). Earlier, G18.937−0.434 was labeled as G018.937−0.434a (hydrogen RRL $V_{lsr}$ ∼68 km s$^{-1}$) and G018.937−0.434b (hydrogen RRL $V_{lsr}$ ∼36.2 km s$^{-1}$) in the source catalog of the Green Bank Telescope H II Region Discovery Survey (GBT HRDS; e.g., Anderson et al. 2011). Wenger et al. (2013) also studied the properties of helium and carbon RRL emission from the HRDS nebulae (including the H II region G018.937−0.434a). Concerning the source G018.937−0.434a, line widths of hydrogen and helium lines were reported to be 23.83±0.05 and 16.31±0.85 km s$^{-1}$, respectively (Wenger et al. 2013), which are smaller than the ones observed in supernova remnants (SNRs; i.e., > 50 km s$^{-1}$; Liu et al. 2019). Based on the properties of RRL emission (i.e., the $^4$He$^+$/H$^+$ ionic abundance ratio and line widths), the G18.937−0.434 (or G018.937−0.434a) was classified as a Galactic H II region. In Figure 1b, we find the absorption features against the Galactic background in the *Spitzer* images, indicating the presence of infrared dark clouds (IRDCs; see dashed arrows in Figure 1b). A majority of the AT-LASGAL clumps at a distance of 5.0 kpc are also seen in the direction of our selected area around G18.88−0.49 (see Figure 1a). Hence, in this paper, we have adopted a distance of 5.0 kpc to the selected H II regions for further analyses.

An object studied earlier IRDC SDC18.8880.476 (hereafter SDC18) from the catalogue of Peretto & Fuller (2009) is also highlighted in Figure 1b. Rigby et al. (2018) presented the 1.2 and 2.0 mm continuum maps of SDC18, which were observed with the IRAM 30 m telescope. Cyganowski et al. (2008) reported an EGO at the centre of SDC18. In general, EGOs are always associated with the extended emission at 4.5 $\mu$m, and are potential candidates for massive protostellar outflows (e.g., Cyganowski et al. 2008). A water maser ($V_{lsr}$ ∼65.1 km s$^{-1}$; Walsh et al. 2011) and a 6.7 GHz methanol maser ($V_{lsr}$ ∼56.4 km s$^{-1}$; Breen et al. 2015; Yang et al. 2019) have also been observed toward SDC18, and the positions of these masers are marked in Figure 1b. In the direction of SDC18, the position of the methanol maser coincides with that of the EGO. Additionally, noticeable YSOs were also reported around G18.88−0.49 (Kerton et al. 2013). Hence, star formation activity has been found toward the site around G18.88−0.49.

Kerton et al. (2013) reported an age difference between the W39 H II region (age ∼1.5 Myr) and the compact H II regions (i.e., G18.88−0.49 and G18.937−0.434; age ∼$10^5$ years). On the basis of the observed morphology of W39 and the age difference argument, they suggested a triggered star formation scenario in W39 (see also Li et al. 2019). They proposed that the H II regions G18.88−0.49 and G18.937−0.434 were triggered by the expansion of the W39 H II region. This interpretation was also supported by Li et al. (2019). However, it is an extremely difficult task to distinguish which stars are triggered and which ones formed spontaneously, and one should be cautious in interpreting observations in favour of triggered star formation (Dale et al. 2015).

In this paper, we examine the region around G18.88−0.49 to search for a hub-filament morphology using a multi-wavelength approach. In this connection, we identify embedded filaments and explore their role in the star formation process in the H II region G18.88−0.49 using the *Herschel* sub-millimeter continuum images and the molecular line data. We also study the nature of the H II regions G18.88−0.49 and G18.937−0.434 using the multi-frequency radio continuum data.

## 3. DATA SETS

The size of the selected region is ∼0°.27 × 0°.27 centered at $l = 18°.857$; $b = −0°.469$, corresponding to a physical scale of ∼23.5 pc × 23.5 pc at a distance of 5.0 kpc (Figure 1a). We used the publicly available "science-ready" observational data products from different surveys summarized in Table 1.

The $^{12}$CO(J =1−0), $^{13}$CO(J =1−0), and C$^{18}$O(J =1−0) line data were retrieved from the FOREST Unbiased Galactic plane Imaging survey with the Nobeyama 45-m telescope (FUGIN; Umemoto et al. 2017) survey, and are calibrated in main beam temperature ($T_{mb}$) (Umemoto et al. 2017). The typical rms noise level[1] is ∼1.5 K, ∼0.7 K, and ∼0.7 K for $^{12}$CO, $^{13}$CO, and C$^{18}$O lines, respectively. The multi-beam receiver, FOur-beam REceiver System on the 45-m Telescope (FOREST; Mi-

[1] https://nro-fugin.github.io/status/

namidani et al. 2016; Nakajima et al. 2019), was utilized for the FUGIN survey. To improve sensitivities, we smoothed the FUGIN data cube with a Gaussian function, giving a spatial resolution of 35″.

We also use radio continuum maps at six different frequencies between 1 and 2 GHz (explicitly, at 1.06, 1.31, 1.44, 1.69, 1.82, and 1.95 GHz) from The HI/OH/Recombination line survey of the inner Milky Way (THOR) (Beuther et al. 2016; Bihr et al. 2016; Wang et al. 2018).

We also explore the *Herschel* temperature and column density maps (resolution ∼12″) produced for the *EU-funded ViaLactea project* (Molinari et al. 2010b). Both maps were generated using the Bayesian *PPMAP* procedure (Marsh et al. 2015, 2017) and downloaded from the publicly available site[2].

## 4. RESULTS

### 4.1. *Physical environment of G18.88−0.49*

#### 4.1.1. *Multi-band view of G18.88−0.49*

We examine the infrared, sub-millimeter (mm), and radio continuum images of G18.88−0.49 to investigate its physical environment (see Figure 2). In Figures 2a–2i, we display images at 3.6 $\mu$m, 8.0 $\mu$m, 70 $\mu$m, 160 $\mu$m, 250 $\mu$m, 350 $\mu$m, 500 $\mu$m, 870 $\mu$m, and 1950 MHz, respectively. The positions of the 6.7 GHz methanol maser and the RRL observations are also marked in the multiwavelength images. The IRDCs seen in the images at 3.6 and 8.0 $\mu$m appear as bright emission regions in the images at 70–870 $\mu$m. As highlighted earlier, SDC18 is associated with the 6.7 GHz methanol maser and the EGO. In the sub-mm images, we find a bright condensation/clump hosting the 6.7 GHz methanol maser/EGO. The *Herschel* and ATLASGAL images show the existence of potential filaments in our target site (see dashed arrows in Figures 2g and 2h). A shell-like feature is also seen in these images (see a contour and a solid arrow in Figure 2g), and appears to be connected with potential filaments (see Sections 4.1.4 and 4.2 for quantitative information). In the direction of the shell-like feature, the NH$_3$ (1,1) emission has been observed (see Figure 6 in Li et al. 2019), suggesting the presence of dense gas (see plus symbols in Figure 2g).

#### 4.1.2. *Dust clumps*

The positions of 17 ATLASGAL dust clumps are also shown in Figure 2h (see empty and filled hexagons). In Table 2, we provide the positions and physical parameters of the clumps from Urquhart et al. (2018). All these clumps are traced in a $V_{lsr}$ range of ∼[61, 67.5] km s$^{-1}$. We also compute the average volume density of each clump as $n_{H_2} = 3M_{clump}/(4\pi R_{clump}^3 \mu_{H_2} m_H)$ (i.e., assuming that they are approximately spherical). Here, $R_{clump}$ is the clump effective radius, $M_{clump}$ is the clump mass, $m_H$ is the mass of a hydrogen atom and the mean molecular weight $\mu_{H_2}$ is assumed to be 2.8. The values of $n_{H_2}$ for all the clumps are also tabulated in Table 2, and vary between ∼2 × 10$^2$ and ∼1.27 × 10$^4$ cm$^{-3}$. We trace a dust temperature range of ∼13.7–25 K. We find 8 clumps with $M_{clump} > 10^3$ M$_\odot$ (see clump IDs with daggers in Table 2).

[2] http://www.astro.cardiff.ac.uk/research/ViaLactea/

In Figure 2h, we also highlight six clumps (see filled hexagons) for which their physical parameters were derived from the NH$_3$ line data from Wienen et al. (2012); such parameters are listed in Table 3. Using these parameters, we also derive the sound speed ($a_s$), thermal velocity dispersion ($\sigma_T$), non-thermal velocity dispersion ($\sigma_{NT}$), Mach number ($M = \sigma_{NT}/a_s$), and ratio of thermal to non-thermal gas pressure ($R_p = a_s^2/\sigma_{NT}^2$; see Lada et al. 2003, for more details). These parameters are also included in Table 3. The value of the sound speed $a_s$ ($= (kT_{kin}/\mu m_H)^{1/2}$) is computed considering $\mu = 2.37$ (approximately 70% H and 28% He by mass) and the kinematical temperature ($T_{kin}$) as given in Table 3. The non-thermal velocity dispersion is given by the following equation:

$$\sigma_{NT} = \sqrt{\frac{\Delta V^2}{8\ln 2} - \frac{kT_{kin}}{17m_H}} = \sqrt{\frac{\Delta V^2}{8\ln 2} - \sigma_T^2}, \qquad (1)$$

where $\Delta V$ is the measured full width at half maximum (FWHM) linewidth of the observed NH$_3$ spectra, $\sigma_T$ ($= (kT_{kin}/17m_H)^{1/2}$) refers to the thermal broadening for NH$_3$ (e.g. Dunham et al. 2011; Dewangan et al. 2016). The values of $R_p$ range from 0.04 to 0.12 with an average of 0.09 in six clumps, while the range of Mach numbers of these clumps is [2.9, 4.8] with an average of 3.5. These physical parameters suggest that non-thermal pressure and supersonic non-thermal motions (e.g., turbulence, outflows, shocks, and/or magnetic fields) are dominant in these clumps (e.g., Lada et al. 2003).

#### 4.1.3. *Radio sources*

Figure 2f displays the overlay of the NVSS 1.4 GHz continuum emission contours (beam size ∼45″; noise level ∼0.45 mJy beam$^{-1}$; Condon et al. 1998) on the *Herschel* 350 $\mu$m image. In the NVSS map, radio clumps are clearly seen toward the H II regions G18.88−0.49 and G18.937−0.434. However, no radio continuum peak is seen toward the position of the 6.7 GHz methanol maser. Using the *clumpfind* IDL program (Williams et al. 1994), we estimated the integrated fluxes at NVSS 1.4 GHz of the radio sources containing these H II regions. Using the integrated flux at NVSS 1.4 GHz, we computed the number of Lyman continuum photons ($N_{UV}$) and the dynamical age ($t_{dyn}$) of each H II region. Following the equations and analysis adopted in Dewangan et al. (2017a), we compute the value of log $N_{UV}$ to be 48.22 and 47.90 for the H II regions G18.88−0.49 and G18.937−0.434, respectively (see Matsakis et al. 1976, for equations). Based on these values, the H II regions G18.88−0.49 and G18.937−0.434 are excited by O9V–O9.5V and O9.5V–B0V stars, respectively (e.g., Panagia 1973). Considering the typical value of the initial particle number density of the ambient neutral gas ($n_0 = 10^3$ (10$^4$) cm$^{-3}$), the dynamical age of the H II regions G18.88−0.49 and G18.937−0.434 is estimated to be ∼0.4 (1.4) and ∼0.4 (1.3) Myr, respectively (e.g., Dyson & Williams 1980). Kerton et al. (2013) also reported similar ages and spectral types of the powering stars of both the H II regions. The electron temperature of 10$^4$ K, the isothermal sound velocity in the ionized gas (= 11 km s$^{-1}$; Bisbas et al. (2009)), and the distance of 5 kpc are adopted in this calculation. The analysis assumes that

**Table 1**
List of different surveys utilized in this paper.

| Survey | Wavelength/Frequency/line(s) | Resolution ($''$) | Reference |
|---|---|---|---|
| Multi-Array Galactic Plane Imaging Survey (MAGPIS) | 20 cm | $\sim$6 | Helfand et al. (2006) |
| The HI/OH/Recombination line survey of the inner Milky Way (THOR) | 1–2 GHz | $\sim$25 | Beuther et al. (2016) |
| NRAO VLA Sky Survey (NVSS) | 21 cm | $\sim$45 | Condon et al. (1998) |
| FUGIN survey | $^{12}$CO, $^{13}$CO, C$^{18}$O (J = 1–0) | $\sim$20 | Umemoto et al. (2017) |
| APEX Telescope Large Area Survey of the Galaxy (ATLASGAL) | 870 $\mu$m | $\sim$19.2 | Schuller et al. (2009) |
| *Herschel* Infrared Galactic Plane Survey (Hi-GAL) | 70–500 $\mu$m | $\sim$5.8–37 | Molinari et al. (2010a) |
| *Spitzer* MIPS Inner Galactic Plane Survey (MIPSGAL) | 24 $\mu$m | $\sim$6 | Carey et al. (2005) |
| *Spitzer* Galactic Legacy Infrared Mid-Plane Survey Extraordinaire (GLIMPSE) | 3.6–8.0 $\mu$m | $\sim$2 | Benjamin et al. (2003) |

the H II regions are uniform and spherically symmetric.

The THOR survey provides six radio continuum maps at 1–2 GHz (beam size $\sim$25$''$; noise level $\sim$0.3–1 mJy beam$^{-1}$; Bihr et al. 2016) and spectral index of radio sources. The THOR maps at 1–2 GHz have a better resolution and sensitivity than the NVSS map at 1.4 GHz. In Figure 2i, we show the THOR 1950 MHz continuum map overlaid with the THOR 1950 MHz continuum contours. Figures 2f and 2i allow us to compare the observed radio emission of the H II regions G18.88−0.49 and G18.937−0.434. In the THOR 1950 MHz continuum map, we see several peaks that are not detected in the NVSS radio continuum map. We also do not find any radio continuum peak toward the position of the 6.7 GHz methanol maser in the continuum map at 1950 MHz. The positions of the ATLASGAL clumps are also highlighted in the THOR continuum map, allowing us to compare the positions of the dust clumps with the ionized emission.

In Figure 2i, the positions of the radio continuum sources from the THOR survey are also marked. The spectral index is measured using the radio peak fluxes at 1.06, 1.31, 1.44, 1.69, 1.82, and 1.95 GHz (e.g., Bihr et al. 2016). The determination of the value of $\alpha$ helps us to infer whether the radio continuum emission is thermal or non-thermal (e.g., Rybicki & Lightman 1979; Longair 1992). Thermally emitting sources show a positive or near zero spectral index. SNRs exhibit non-thermal emission with $\alpha \approx -0.5$, while extragalactic objects generally have a steeper $\alpha \approx -1$ (e.g., Bihr et al. 2016). Based on the values of $\alpha$, two THOR sources G18.875−0.360 ($\alpha \sim -1.05$) and G18.755−0.497 ($\alpha \sim -0.77$) are more likely to be extragalactic objects. The H II region G18.88−0.49 ($\alpha \approx 0.09$) shows thermal radio continuum emission, while the H II region G18.937−0.434 ($\alpha \approx -0.4$), powered by an O-type star, displays non-thermal radio continuum emission (see Section 5.2 for more details). Despite the value of $\alpha \approx -0.4$, the source G18.937−0.434 was reported as an H II region and not a SNR candidate (see source G18.939−0.443 in Wang et al. 2018). As mentioned earlier, this source was also classified as a Galactic H II region (Anderson et al. 2011; Wenger et al. 2013). The observed spectral index of $\approx -0.4$ is consistent with a combination of thermal and non-thermal emission. The estimation of the spectral type of the powering source of this H II region appears to be overestimated because the total radio continuum flux of the H II region has been treated as thermal emission (see also Section 5.2).

### 4.1.4. *Herschel temperature and column density maps*

Figure 3a shows the *Herschel* temperature ($T_{\rm d}$) map of our selected target area around G18.88−0.49. We find the presence of warm dust emission ($T_{\rm d}$ = 23.5–25.5 K) toward both H II regions, G18.88−0.49 and G18.937−0.434. In Figure 3b, we display the *Herschel* column density ($N(\rm H_2)$) map overlaid with the $N(\rm H_2)$ contours at [14.1, 21] × 10$^{21}$ cm$^{-2}$. Here, to trace different features in the *Herschel* column density map, we employ different $N(\rm H_2)$ contour levels through visual examination. The $N(\rm H_2)$ contour at 14.1 × 10$^{21}$ cm$^{-2}$ enables us to trace potential filaments in our selected target area. In the column density map, we identify the shell-like feature (extension $\sim$12 pc × 7 pc) at $N(\rm H_2)$ = 21 × 10$^{21}$ cm$^{-2}$ (see the black contour in Figure 3b; and also Section 4.1.1). The existence of the shell-like feature is also confirmed by the previously published NH$_3$ (1,1) line data (see plus symbols in Figure 2g), which is associated with the dense gas. With the help of the *Herschel* $N(\rm H_2)$ map, the total mass of the shell-like feature is determined to be $\sim$2.9 ×10$^4$ M$_\odot$ using the equation $M_{area} = \mu_{H_2} m_H A_{pix} \Sigma N(H_2)$, where $\mu_{H_2}$ is defined earlier (i.e., 2.8), $A_{pix}$ is the area subtended by one pixel (i.e., 6$''$/pixel), and $\Sigma N(H_2)$ is the total column density (see also Dewangan et al. 2017a, for more details of the analysis). The *clumpfind* IDL program is employed to estimate the value of $\Sigma N(H_2)$ (e.g., Dewangan et al. 2017c, 2018b).

In Figure 3c, we display a color-composite map with the *Spitzer* 8.0 $\mu$m and the THOR 1950 MHz images. One of the MIR bubbles (MWP-1G018879-004949 (radius = 1$'$.53)) surrounds the H II region G18.88−0.49. In other words, the MIR bubble is filled with the ionized gas. The color-composite map is also overlaid with the $N(\rm H_2)$ contours at [14.1, 26.4] × 10$^{21}$ cm$^{-2}$. At $N(\rm H_2)$ = 26.4 × 10$^{21}$ cm$^{-2}$, we identify at least four subregions around the H II region G18.88−0.49, which are labeled as A (mass $\sim$10.5 ×10$^3$ M$_\odot$), B (mass $\sim$8 ×10$^3$ M$_\odot$), C (mass $\sim$1.1 ×10$^3$ M$_\odot$), and D (mass $\sim$0.8 ×10$^3$ M$_\odot$). We followed the same steps as mentioned above to estimate the total mass of each sub-region. In Figure 3d, we highlight five potential filaments (fk, fl, fm, fn, and fo) having typical lengths of five to eight parsecs, the shell-like feature, and four subregions (see also Section 4.2.1). These proposed filaments, which have low column density, are associated with the shell-like feature having high column density. The association of the proposed filaments and the shell-like feature reveals an interesting configuration similar to a "hub-filament" system (e.g., Myers 2009; Schneider et al. 2012; Baug et al. 2015; Dewangan et al. 2015, 2016, 2018a). We find that the ends of the proposed filaments, which are approaching the hub, are associated

with the dense parts of the shell-like feature. This finding is further explored using the analysis of the molecular line data in Section 4.2. The H II region G18.88−0.49 excited by an O-type star is seen almost at the center of the shell-like feature, where no dust emission at $N(H_2) = 21 \times 10^{21}$ cm$^{-2}$ is detected (see Figures 3c and 3d). These findings suggest that the energetics of a young massive O-type star (e.g., ionizing radiation, stellar winds, and radiation pressure) might have interacted with its immediate surroundings. Additionally, some radio peaks are seen toward this shell-like feature (see subregions A, B and C). Furthermore, the H II region G18.937−0.434 does not appear to be part of the hub-filament system.

## 4.2. Morphology of molecular cloud and kinematics of molecular gas

### 4.2.1. Moment and velocity channel maps

We extracted $^{13}$CO spectra toward nine small fields (i.e., t1–t9) that are highlighted in Figure 3d. These are selected toward the regions around the shell-like feature. Figures 4a–4i present the averaged $^{13}$CO spectra toward nine small fields t1–t9. The spectra show that the molecular gas is well traced in a velocity range of [60, 70] km s$^{-1}$, confirming the existence of a single velocity component in the direction of our selected target site.

To infer the morphology of the molecular cloud associated with the target site, the integrated $^{12}$CO, $^{13}$CO, and C$^{18}$O intensity maps (or moment-0 maps) are presented in Figures 5a, 5b, and 5c, respectively. The molecular gas is integrated in a velocity range of [60.2, 70.6] km s$^{-1}$. In Figure 5b, the column density contour at $14.1 \times 10^{21}$ cm$^{-2}$ is shown to highlight the proposed Herschel filaments. The black contour (at $N(H_2) = 21 \times 10^{21}$ cm$^{-2}$) represents the shell-like feature in Figure 5b. The $^{13}$CO emission follows quite well the morphology of the shell-like feature as investigated in the Herschel column density map. The moment-0 maps of $^{12}$CO and C$^{18}$O also trace the shell-like feature, which is also well depicted by the dense gas tracer NH$_3$ (see plus symbols in Figure 5c). The C$^{18}$O and NH$_3$ emissions are not very strong toward the proposed filaments, indicating that these filaments are not very dense compared to the shell-like feature. However, low intensity $^{13}$CO emission is clearly seen toward all these filaments at $N(H_2) = 14.1 \times 10^{21}$ cm$^{-2}$ (see a thin contour in Figure 5b). No molecular emission is found toward the other H II region G18.937−0.434.

The moment-1 maps (i.e., the intensity-weighted central velocity) of the $^{12}$CO, $^{13}$CO, and C$^{18}$O emission are shown in Figures 5d, 5e, and 5f, respectively. Based on the comparison of the moment-1 maps to the integrated intensity maps, one can depict the noticeable velocity variations toward different parts of the shell-like feature. In Figures 5e and 5f, we see a noticeable sharp border between the two velocity fields toward the shell-like feature, revealing a velocity gradient.

In Figure 6a, we highlight different axes (i.e., "i1–i2", "j1–j2", "k1–k2", "l1–l2", "m1–m2", "n1–n2", and "o1–o2") in the integrated intensity map of $^{13}$CO. Along each of these axes, a position-velocity diagram is presented in Figure 9. The axes "i1–i2" and "j1–j2" are selected in the direction of the major and minor axes of the shell-like feature, respectively. Figure 6b presents a zoomed-in area around the shell-like feature using a color-composite

map with the moment-0 map of $^{13}$CO and the THOR 1950 MHz images. Here, the moment-0 map of $^{13}$CO is processed through an edge detection algorithm (i.e. Difference of Gaussian (DoG); see Gonzalez & Woods 2011; Assirati et al. 2014; Dewangan et al. 2017b). It enables us to visually probe five filaments (i.e., fk, fl, fm, fn, and fo) as seen in the Herschel column density map (see Figure 3d). The ionized gas is distributed almost at the center of the shell-like feature (extension ~12 pc × 7 pc; aspect ratio ~1.7), which is well traced with the NH$_3$ emission (see plus symbols). The aspect ratios of the selected five molecular filaments vary between 2.3 to 4. Hence, this molecular map supports the existence of the hub-filament system around the H II region G18.88−0.49. Figure 6c displays the hub-filament system overlaid with the positions of the ATLASGAL clumps, the shell-like feature, and the filaments. The positions of Class I YSOs and flat-spectrum sources are also marked in Figure 6c. The identification of these YSOs is discussed in Section 4.3.

Figure 7 displays the integrated $^{13}$CO velocity channel maps (starting from 56.3 km s$^{-1}$ at intervals of 1.3 km s$^{-1}$). In Figure 8, we present the velocity channel maps of the C$^{18}$O emission (starting from 59.6 km s$^{-1}$). In Figures 7 and 8, the shell-like feature and four Herschel subregions ("A–D") are also highlighted. Both channel maps trace the shell-like feature, and it appears that some parts of the shell-like feature appear clumpy (i.e., subregions). The $^{13}$CO and C$^{18}$O gas motion is also evident in the shell-like feature (including the Herschel subregions). The higher intensity of C$^{18}$O is found toward the sub-region "B", while the sub-region "A" is traced with the higher intensity of $^{13}$CO. In Figure 7, the $^{13}$CO emission is also seen toward all the proposed filaments (see five solid lines and also the panel at [66.7, 68.0] km s$^{-1}$).

### 4.2.2. Position-velocity diagrams along filaments

In this section, we produce the position-velocity diagrams of $^{13}$CO to explore the velocity structure of the filaments. Figures 9a, 9b, 9c, 9d, 9e, 9f, and 9g show the position-velocity diagrams of $^{13}$CO along the axes "i1–i2", "j1–j2", "k1–k2", "l1–l2", "m1–m2", "n1–n2", and "o1–o2", respectively. In these axes, the positions k2, l2, m2, n2, and o2 are selected toward the central hub. In direction of the shell-like feature (see Figures 9a and 9b), a velocity spread is observed. Figures 9c, 9d, 9e, 9f, and 9g show the existence of velocity gradients (about 0.8–1.8 km s$^{-1}$ pc$^{-1}$) along the filaments fk, fl, fm, fn, and fo, respectively. The end of each filament that reaches the hub is associated with the dense parts of the shell-like feature (see the positions k2, l2, m2, n2, and o2 in Figure 6). The implication of the hub-filament configuration concerning the star formation process in G18.88−0.49 is presented in Section 5.

### 4.3. Star formation activity

Kerton et al. (2013) identified YSOs using the Spitzer photometric data at 3.6–24 $\mu$m in W39, and provided the positions and photometric magnitudes of 36 YSOs (see Table 1 in their paper). We find only 19 out of 36 YSOs (6 Class I; 7 Class I/II; 6 Class II) that are restricted upto a small area of our selected tar-

get region (see a dotted yellow box in Figure 10a). Hence, we also identified infrared-excess sources/YSOs in our entire selected area around G18.88−0.49 using the Spitzer photometric data at 3.6–24 μm. In this connection, three schemes are employed in this paper, which are color-magnitude plot ([3.6]−[24] vs [3.6]), color-color plot ([3.6]−[4.5] vs [5.8]−[8.0]), and color-color plot ([4.5]−[5.8] vs [3.6]−[4.5]). One can find more details of these schemes in Dewangan et al. (2017d, 2018a). We obtained photometric magnitudes of point-like sources at Spitzer 3.6–8.0 μm bands from the GLIMPSE-I Spring' 07 highly reliable catalog. Furthermore, photometric magnitudes of sources at Spitzer 24 μm were also retrieved from the publicly available MIPSGAL catalog (e.g., Gutermuth & Heyer 2015).

Using the color-magnitude plot ([3.6]−[24] vs [3.6]; not shown here), different evolutionary stages of YSOs (i.e., Class I, flat-spectrum, and Class II) are identified against the possible contaminants (i.e., galaxies and disk-less stars; see Guieu et al. 2010; Rebull et al. 2011). Note that this particular YSO identification and classification scheme was not used by Kerton et al. (2013). With the application of this highlighted scheme, we find 15 YSOs (3 Class I; 2 flat-spectrum; 10 Class II) in our selected target area. In Figure 10a, we overlay the positions of Class I, flat-spectrum, and Class II YSOs on the moment-0 map of $^{13}$CO, which are indicated by black filled circles, yellow filled diamonds, and yellow filled triangles, respectively.

Using the color-color plot ([3.6]−[4.5] vs [5.8]−[8.0]; not shown here), different evolutionary stages of YSOs (i.e., Class I and Class II) are selected against various contaminants (such as PAH-emitting galaxies and PAH-emission-contaminated apertures). Following the methods reported in Gutermuth et al. (2009) and Lada et al. (2006), the selected YSOs and various contaminants are identified. With the help of this scheme, we find 22 YSOs (6 Class I; 16 Class II) in our selected target area. These selected YSOs are not common with the YSOs identified using the Spitzer color-magnitude plot ([3.6]−[24] vs [3.6]). In Figure 10a, the positions of the selected Class I and Class II YSOs are marked by magenta filled circles and triangles, respectively.

Using the color-color plot ([4.5]−[5.8] vs [3.6]−[4.5]; not shown here), we identify Class I YSOs with the infrared color conditions (i.e. [4.5]−[5.8] ≥ 0.7 mag and [3.6]−[4.5] ≥ 0.7 mag) given in Hartmann et al. (2005) and Getman et al. (2007) (see also Dewangan et al. 2020b). Using this scheme, we select 13 Class I YSOs. These YSOs are not matched with the ones, which are identified in the above discussed two schemes. One can notice that this highlighted scheme was not utilized by Kerton et al. (2013). In Figure 10a, the positions of the selected Class I YSOs are indicated by white filled circles.

Taken together, these three schemes yield a total of 50 YSOs (22 Class I; 2 flat-spectrum; 26 Class II) in our selected target field. In Figures 10b, these YSOs are also overlaid on the Spitzer color-composite image. Hence, one can examine the spatial distribution of all these YSOs in Figures 10a and 10b. Kerton et al. (2013) identified 6 Class I YSOs toward the area highlighted by a dotted yellow box in Figure 10a, and 5 out of these 6 Class I YSOs are in agreement with the present work. However, the remaining one Class I YSO is classified as a flat-spectrum source in this paper. No noticeable YSOs are seen toward the proposed filaments. We do not find YSOs toward the bubble MWP-1G018848-004761, while the Class I YSOs, EGO, water maser, and 6.7 GHz methanol maser are seen toward the MIR bubble MWP-1G018879-004949 surrounding the H ɪɪ region G18.88−0.49.

There are 11 ATLASGAL clumps (c3–c13; see Table 2), 8 Class I YSOs, and 1 flat-spectrum source distributed toward the shell-like feature (see filled circles and filled diamonds in Figure 6c). Furthermore, the 6.7 GHz methanol maser and the EGO are associated with the clump c11 ($L_{bol}$ ∼53.8 × $10^3$ $L_{\odot}$; $M_{\mathrm{clump}}$ ∼4880 $M_{\odot}$; see Table 2) and a Class I YSO (GLIMPSE catalog ID: G018.8885−00.4746). In Figure 10c, we display a zoomed-in view of an area around the H ɪɪ region G18.88−0.49 and SDC18 using the Spitzer 24 μm image. The image is also overlaid with the IRAM 1.2 mm continuum emission contours (resolution ∼ 13″) from Rigby et al. (2018) and the THOR 1950 MHz continuum contours. The Class I YSO is also well detected in the Spitzer 24 μm image, and is seen toward the dust continuum peak at IRAM 1.2 mm. This source can be considered as an infrared counterpart (IRc) of the 6.7 GHz methanol maser emission, and is found toward the EGO (e.g., Cyganowski et al. 2008). Hence, this source is associated with the outflow activity. In general, the 6.7 GHz methanol maser (<0.1 Myr) is thought to be a reliable tracer of massive young stellar objects (MYSOs) (e.g. Walsh et al. 1998; Minier et al. 2001; Urquhart et al. 2013). Hence, the IRc associated with the clump c11 may be a MYSO candidate (stellar mass ∼7.7 M$_{\odot}$; see source ID #G18-2 in Table 3 in Kerton et al. 2013) going through an accretion phase. There is no radio peak seen toward the IRc (see Figure 10c). Hence, it could be a genuine MYSO in a very early evolutionary stage, prior to an ultracompact (UC) H ɪɪ phase. Note that the position of the H ɪɪ region G18.88−0.49 is located away from that of the 6.7 GHz methanol maser (see Figure 10c), suggesting the existence of different early evolutionary stages of massive star formation in the shell-like feature. It seems that other Class I YSOs could be low-mass stars. The average age of Class I YSOs has been reported to be ∼0.44 Myr (Evans et al. 2009).

Together, the distribution of the selected Class I YSOs, a MYSO candidate, and a young O-type star in the H ɪɪ region G18.88−0.49 (age ∼$10^5$ years for $n_0 = 10^3$ cm$^{-3}$) traces the early stage of star formation (including massive stars) toward the shell-like feature.

## 5. DISCUSSION

### 5.1. Star formation scenario in G18.88−0.49

One of the important findings of the Herschel Space Observatory is the identification of numerous networks of filaments constituting hub-filament systems, which are gaining increasing attention as the most appropriate places for forming massive stars and star clusters (Motte et al. 2018; Kumar et al. 2020). In the literature, several star-forming regions are reported to have a hub-filament system, namely Taurus (Myers 2009), Ophiuchus (Myers 2009), Rosette (Schneider et al. 2012), SDC335.579-0.292 (Peretto et al. 2013), IRDC G14.225−0.506 (Busquet et al. 2013), Sh 2-138 (Baug et al. 2015), W42

(Dewangan et al. 2015), IRAS 05480+2545 (Dewangan et al. 2017b), Sh 2-53 (Baug et al. 2018), and Monoceros R2 (Treviño-Morales et al. 2019). In the IRDC G14.225−0.506, Busquet et al. (2013) identified two hub-filament systems using the $NH_3$ line data, and provided a table containing the aspect ratios of filaments and hubs to be 7.3–27.8 and 4.9–5, respectively (see Table 1 in their paper). Hence, in the hub-filament systems, hubs are more compact and dense compared to filaments.

It has also been proposed that hub-filament systems are the reliable sites for massive star formation, and the gas flows through the filaments are responsible for the central hub (e.g., Tigé et al. 2017; Motte et al. 2018; Kumar et al. 2020). In the relation of ridges/hubs, Tigé et al. (2017) presented a scenario for the formation of massive stars (see their Figure 8 and also Motte et al. 2018). Treviño-Morales et al. (2019) also discussed this scenario in support of their observational results in Monoceros R2. Firstly, in this scheme, Tigé et al. (2017) and Motte et al. (2018) highlighted a molecular cloud complex hosting a hub/ridge filament system with gas flowing via the filaments to the central hub, where massive dense cores/clumps (MDCs, in a 0.1 pc scale) develop. During their starless phase ($\sim 10^4$ yr), only low-mass prestellar cores are expected in MDCs. The MDCs become protostellar when containing a stellar embryo of low mass ($\sim 3\times10^5$ yr). Then, the protostellar envelopes feed from the gravitationally-driven inflows, allowing the birth of massive protostars. Massive protostars become infrared-bright for stellar embryos with masses greater than 8 $M_\odot$. Finally, the main accretion phase halts when the stellar UV radiation ionizes the protostellar envelope and generates an H II region (in a time of few $10^5$–$10^6$ yr).

The analysis of the *Herschel* column density map and the molecular line data has allowed us to uncover the physical environment of G18.88−0.49. These data sets show the existence of a massive shell-like feature (mass $\sim 2.9 \times 10^4$ $M_\odot$; extension $\sim$12 pc × 7 pc; aspect ratio $\sim$1.7) and five filaments (i.e., fk, fl, fm, fn, and fo; aspect ratio $\sim$2.3–4) having typical length of five to eight parsecs in the selected site around G18.88−0.49. It implies that filaments have high aspect ratio and lower column densities ($\sim 10^{21}$ cm$^{-2}$), while the shell-like feature is associated with dense gas, and has low aspect ratio and high column density ($\sim 10^{22}$ cm$^{-2}$). The physical association of the filaments and the shell-like feature reveals a hub-filament system around the H II region G18.88−0.49 (see Sections 4.1.4 and 4.2). These are the key and new results in G18.88−0.49.

In this work we investigated four *Herschel* subregions toward the shell-like feature with masses of $\sim$0.8–10.5 $\times 10^3$ $M_\odot$, which are also traced by the $C^{18}O$ and $NH_3$ emission (see Figure 5c). In the direction of these subregions, we find dense clumps dominated by non-thermal pressure and supersonic non-thermal motions (see Sections 4.1.2 and 4.1.4). The shell-like feature is associated with the H II region G18.88−0.49, a MYSO candidate, and low-mass Class I YSOs (mean age $\sim$0.44 Myr; Evans et al. 2009). All these results reveal the ongoing star formation activity in the shell-like feature (see Section 4.3). The center of the shell-like feature appears to be influenced by the energetics of the massive O-type star powering the H II region G18.88−0.49, which is surrounded by

the MIR bubble MWP-1G018879-004949. However, this H II region (age $\sim 10^5$ years) is not old enough to trigger a new generation of stars. Hence, this paper focuses to understand the role of observed features (i.e., filaments and shell-like feature) in physical processes involved in star formation in G18.88−0.49.

We find five parsec-scale filaments that appear to be radially directed to the dense parts/subregions of the shell-like feature (see Figure 6c). The FUGIN $^{13}CO$ line data have been examined to study the velocity structure of the filaments (see Section 4.2). Based on the position-velocity analysis of $^{13}CO$, we find noticeable velocity gradients (0.8–1.8 km s$^{-1}$ pc$^{-1}$) along five filaments (see Figure 9). These velocity gradients are similar to those reported in NGC 1333 ($\sim$0.5 – 2.5 km s$^{-1}$ pc$^{-1}$; Hacar et al. 2017), Serpens South SF region (1.4 km s$^{-1}$ pc$^{-1}$; Kirk et al. 2013), and Monoceros R2 ($\sim$0.0 – 0.8 km s$^{-1}$ pc$^{-1}$; Treviño-Morales et al. 2019). The observation of velocity gradients along molecular filaments is considered as a signpost of gas accreting along these filaments, which also feed star-forming cores and proto-clusters in the central hub (e.g., Kirk et al. 2013; Nakamura et al. 2014; Olmi et al. 2016; Treviño-Morales et al. 2019; Chen et al. 2020). It has also been reported that the molecular gas might be accelerating when entering the hub (e.g., Treviño-Morales et al. 2019). In the direction of the shell-like feature, our results show that the H II region G18.88−0.49 has been formed, while the IRc of the 6.7 GHz methanol maser (i.e., MYSO candidate) is being formed (see Figure 10c). Hence, it is possible that the five filaments fk, fl, fm, fn, and fo had feeded and/or are feeding the central hub, where high $N(H_2)$ materials ($\geq$ 21 × $10^{21}$ cm$^{-2}$) and dense parts/subregions are observed. Our selected target system does not appear a classical "hub-filament" system observed in Monoceros R2 (Treviño-Morales et al. 2019). Based on our observed findings, we can put our proposed hub-filament system in the phases of the infrared-bright massive protostar and the H II region as discussed in the scheme of Tigé et al. (2017) and Motte et al. (2018).

Considering our observed outcomes, we find the applicability of a global non-isotropic collapse scenario in the H II region G18.88−0.49, which includes the flavours of the mentioned global hierarchical collapse and clump-feed accretion scenarios. Hence, the global non-isotropic collapse scenario can explain the observed morphology and star formation in and around G18.88−0.49.

### 5.2. *Radio emission in G18.937−0.434*

The THOR and the NVSS radio continuum maps clearly trace the prominent H II region G18.937−0.434 (see Figures 2f, 2i, and 3c). The *Herschel* maps show the presence of material with $N(H_2) = 11.5$–$13.5 \times 10^{21}$ cm$^{-2}$ and warm dust ($T_d$ = 23–25 K) around this H II region (see Figures 3a and 3b). An arc-like feature is also seen around this H II region in the *Spitzer* 8.0 $\mu$m image (see Figures 2b and 3c). In Figure 10d, we present a zoomed-in view of an area around the H II region G18.937−0.434 using the *Spitzer* 24 $\mu$m image overlaid with the THOR 1950 MHz continuum contours. We find a noticeable MIR emission around the H II region G18.937−0.434, which coincides with the radio continuum emission. However, no noticeable molecular emis-

sion at [60, 70] km s$^{-1}$ is observed toward the H II region G18.937$-$0.434.

Based on an examination of the catalog of THOR radio continuum sources in our selected target area, we find the H II region G18.937$-$0.434 with a negative spectral index ($\alpha \approx -0.4$; see Section 4.1.3), which was produced using the radio peak fluxes at 1–2 GHz. We computed the integrated flux of G18.937$-$0.434 at each of the six THOR bands between 1 GHz and 2 GHz, and fitted the data with a single power-law component, leading to a spectral index $\alpha \approx -0.52$. One can consider about 10% error in the values of flux and $\alpha$. The negative $\alpha$ value indicates non-thermal (synchrotron) radio emission from G18.937$-$0.434, thus revealing the presence of relativistic electrons. Note that we expect a composite spectrum including a thermal component as well, likely produced by the ionized gas, but the limited bandwidth of the radio observations does not allow us to properly disentangle these emission components. Nonetheless, the non-thermal emission has a negative spectral index and it should dominate at low frequencies, whereas the thermal emission is more prominent at higher frequencies. Hence, to interpret the detection of synchrotron emission we focus on the flux value at the lowest frequency accessible in the THOR survey, $S_{1.06 \text{ GHz}} = 1.135$ Jy, as the thermal contamination should be lowest in this band. Assuming that the thermal emission is optically thin (spectral index equal to $-0.1$) and that the non-thermal emission has a spectral index between $-0.5$ and $-1$, the thermal emission at 1.06 GHz is estimated to be $< 0.2 - 0.6$ Jy. If we consider the total thermal flux $S_{1.06 \text{ GHz}} = 0.2(0.6)$ Jy of the H II region G18.937$-$0.434 then it can be excited by a spectral type of B0.5V–B0V (B0V–O9.5V) star (see Section 4.1.3 for the analysis details). Hence, we suggest that the H II region G18.937$-$0.434 is powered by an early B-type main-sequence star.

We adopt the same approach as Dewangan et al. (2020a) for modelling the non-thermal radio emission from an H II region. Taking as a reference a non-thermal spectral index of $\sim -0.8$ as Dewangan et al. (2020a), the non-thermal flux at 1.06 GHz is $\sim$0.7 Jy. We set the ratio between the energy density in relativistic protons and electrons to 100 and assume a minimum-energy condition for the non-thermal particles and the magnetic field. Our analysis yields an energy density of non-thermal particles of $U_{\text{NT}} \sim 34$ eV cm$^{-3}$ and a magnetic field intensity in the H II region of $\sim 43$ $\mu$G. The required value of $U_{\text{NT}}$ greatly exceeds the Galactic cosmic ray energy density ($U_{\text{GCR}} \approx 1$ eV cm$^{-3}$). We conclude that the observed synchrotron flux is produced by relativistic particles locally accelerated in shocked regions of gas, consistent with recent non-thermal emission models (Padovani et al. 2019). However, we still need more observations in frequency ranges below 1 GHz and above 2 GHz to make more robust estimates of the magnetic field and energy particle distribution in this H II region.

## 6. SUMMARY AND CONCLUSIONS

In this paper, we present a detailed multi-wavelength analysis of an area ($\sim 0°.27 \times 0°.27$) around the H II region G18.88$-$0.49. The major outcomes of this observational work are the following:
• The H II region G18.88$-$0.49 is excited by an O-type main-sequence star (dynamical age $\sim 10^5$ years for $n_0 =$

$10^3$ cm$^{-3}$) and shows thermal emission.
• The H II region G18.937$-$0.434 exhibits a radio spectrum which we interpret as a composite spectrum of thermal and non-thermal emission. The thermal component is consistent with being powered by an early B-type main-sequence star.
• The observed non-thermal radio emission in G18.937$-$0.434 can be explained as synchrotron radiation generated by relativistic particles locally accelerated in shocked regions of gas interacting with an ambient magnetic field of $\sim 43$ $\mu$G.
• A shell-like feature (extension $\sim$12 pc $\times$ 7 pc) around the H II region G18.88$-$0.49 is investigated in the *Herschel* column density map. The distribution of molecular ($^{12}$CO, $^{13}$CO, C$^{18}$O, and NH$_3$) gas at [60, 70] km s$^{-1}$ supports the presence of this shell-like feature.
• The shell-like feature (mass $\sim$2.9 $\times 10^4$ M$_\odot$) contains high column density materials ($\geq 21 \times 10^{21}$ cm$^{-2}$) and at least four subregions ("A–D") having a mass range of $\sim$0.8–10.5 $\times 10^3$ M$_\odot$.
• In the direction of the shell-like feature around the H II region G18.88$-$0.49, 8 Class I YSOs (mean age $\sim$0.44 Myr; Evans et al. 2009), 1 flat-spectrum source, and 11 ATLASGAL clumps (c3–c13) are traced.
• In six ATLASGAL clumps (i.e., c4, c5, and c8–c11), the thermal to non-thermal pressure ratio ranges from 0.04 to 0.12 with a mean of 0.09, and Mach number varies from 2.9 to 4.8 with an average of 3.5. These results indicate that these ATLASGAL clumps, distributed toward the *Herschel* subregions ("A–C"), are dominated by non-thermal pressure and supersonic non-thermal motions.
• One of the ATLASGAL clumps c11 ($L_{bol} \sim$53.8 $\times 10^3$ $L_\odot$; $M_{\text{clump}} \sim$4880 $M_\odot$) hosts the IRc of the 6.7 GHz methanol maser and a Class I YSO, which is away from the H II region G18.88$-$0.49. The 6.7 GHz methanol maser is also associated with the EGO. The IRc appears to be a MYSO candidate (stellar mass $\sim$7.7 M$_\odot$; Kerton et al. 2013) associated with the molecular outflow.
• The early phases of star formation activities (including massive stars) are evident in the shell-like feature.
• Five parsec-scale filaments are found in the *Herschel* column density and molecular maps, and seem to be radially pointed to the dense parts of the shell-like feature. This configuration is considered as a "hub-filament" system.
• Significant velocity gradients (0.8–1.8 km s$^{-1}$ pc$^{-1}$) are traced along the five filaments. These findings favor the molecular gas flow towards the central "hub" along these filaments, feeding the central hub.

Overall, our findings are in agreement with a global non-isotropic collapse scenario as discussed in Motte et al. (2018). This scenario seems to successfully explain the observed star formation activities in our selected site around the H II region G18.88$-$0.49.

## REFERENCES

Anderson, L. D., Bania, T. M., Jackson, J. M., et al. 2009, ApJS, 181, 255

Anderson, L. D., Bania, T. M., Balser, D. S., et al. 2011, ApJS, 194, 32

André, P., Men'shchikov, A., Bontemps, S., et al. 2010, A&A, 518, L102

Assirati, L., Silva, N. R., Berton, L., Lopes, A. A., & Bruno, O. M. 2014, Journal of Physics: Conference Series, 490(1), 2014

Baug, T., Ojha, D. K., Dewangan, L. K., et al. 2015, MNRAS, 454, 4335

Baug, T., Dewangan, L. K., Ojha, D. K., et al. 2018, ApJ, 852, 119

Benjamin, R. A., Churchwell, E., Babler, B. L., et al. 2003, PASP, 115, 953

Beuther, H., Bihr, S., Rugel, M., et al. 2016, A&A, 595, 32

Bihr, S. , Johnston, K. G., Beuther, H., et al. 2016, A&A, 588, 97

Bisbas, T. G., Wünsch, R., Whitworth, A. P., & Hubber, D. A. 2009, A&A, 497, 649

Breen, S. L. et al. 2015, MNRAS, 450, 4109

Busquet, G., Zhang, Q., Palau, A. et al. 2013, ApJ, 764, 26

Carey, S. J., Noriega-Crespo, A., Price, S. D., et al. 2005, BAAS, 37, 1252

Chen, M. C., Di Francesco, J., Rosolowsky, E. et al. 2020, ApJ, 891, 84

Condon, J. J., Cotton, W. D., Greisen, E. W., et al. 1998, AJ, 115, 1693

Cyganowski, C. J., Whitney, B. A., Holden, E., et al. 2008, AJ, 136, 2391

Dale, J. E., Haworth, T. J., Bressert, E. 2015, MNRAS, 450, 1199

Dewangan, L. K., Luna, A., Ojha, D. K., et al. 2015, ApJ, 811, 79

Dewangan, L. K., Ojha, D. K., Luna, A., et al. 2016, ApJ, 819, 66

Dewangan, L. K., Ojha, D. K., Zinchenko, I., Janardhan, P., & Luna, A. 2017a, ApJ, 834, 22

Dewangan, L. K., Ojha, D. K., & Baug, T. 2017b, ApJ, 844, 15

Dewangan, L. K., Devaraj, R., Baug, T., & Ojha, D. K. 2017c, ApJ, 848, 51

Dewangan, L. K., Ojha, D. K.,& Zinchenko, I. 2017d, ApJ, 851, 140

Dewangan, L. K., Baug, T., Ojha, D. K., Ghosh, S. K. 2018, ApJ, 869, 30

Dewangan, L. K., Baug, T., Ojha, D. K., Zinchenko, I., Luna, A. 2018b, ApJ, 864, 54

Dewangan, L. K., Sharma, Saurabh, Pandey, R., del Palacio, S., Ojha, D. K., Benaglia, P., Baug, T., & Das, S. R. 2020a, ApJ, in press, arXiv:2006.03244

Dewangan, L. K., Baug, T., & Ojha, D. K. 2020b, MNRAS, 496, 1278

Dunham, M. K., Rosolowsky, E., Evans, II N. J., Cyganowski, C., & Urquhart, J. S. 2011, ApJ, 741, 110

Dyson, J. E., & Williams, D. A. 1980, Physics of the interstellar medium, New York, Halsted Press, 204 p

Evans, N. J., II, Dunham, M. M., Jørgensen, J. K., et al. 2009, ApJS, 181, 321

Getman, K. V., Feigelson, E. D., Garmire,G., Broos, P., & Wang, J. 2007, ApJ, 654, 316

Gonzalez, R, & Woods, R. 2011, *Digital Image Processing* (Pearson Education) ISBN 9780133002324

Guieu, S., Rebull, L. M., Stauffer, J. R., et al. 2010, ApJ, 720, 46

Gutermuth, R. A., Megeath, S. T., Myers, P. C., et al. 2009, ApJS, 184, 18

Gutermuth, R. A., & Heyer, M. 2015, AJ, 149, 64

Hacar, A., Tafalla, M., & Alves, J. 2017, A&A, 606, A123

Hartmann, L., Megeath, S. T., Allen, L., et al. 2005, ApJ, 629, 881

Helfand, D. J., Becker, R. H., White, R. L., Fallon, A., & Tuttle, S. 2006, AJ, 131, 2525

Kerton, C. R., Arvidsson, K., & Alexander, M. J. 2013, AJ, 145, 78

Kirk, H., Myers, P. C., Bourke, T. L., et al. 2013, ApJ, 766, 115

Kumar, M. S. N., Palmeirim, P., Arzoumanian, D., & Inutsuka, S. I. 2020, accepted in A&A, arXiv:2008.00295

Lada, C. J., Bergin, E. A., Alves, J. F., & Huard, T. L. 2003, ApJ, 586, 286

Lada, C. J., Muench, A. A., Luhman, K. L., et al. 2006, AJ, 131, 1574

Li, Xu, Esimbek, J., Zhou, J., et al. 2019, MNRAS, 487, 1517

Liu, B., Anderson, L. D., McIntyre, T., et al. 2019, ApJS, 240, 14

Lockman, F. J. 1989, ApJS, 71, 469

Longair, M. S. 1992, High energy astrophysics. Vol.1: Particles, photons and their detection, 436

Marsh, K. A., Whitworth, A. P., & Lomax, O. 2015, MNRAS, 454, 4282

Marsh, K. A., Whitworth, A. P., Lomax, O., et al. 2017, MNRAS, 471, 2730

Matsakis, D. N., Evans, N. J., II, Sato, T., & Zuckerman, B. 1976, AJ, 81, 172

Minamidani, T. et al., 2016, Development of the new multi-beam100 GHz band SIS receiver FOREST for the Nobeyama 45-mTelescope. p. 99141Z, doi:10.1117/12.2232137

Minier, V., Conway, J. E., & Booth, R. S. 2001, A&A, 369, 278

Molinari, S., Swinyard, B., Bally, J., et al. 2010a, A&A, 518, L100

Molinari, S., Swinyard, B., Bally, J., et al. 2010b, PASP, 122, 314

Motte, F., Bontemps, S., & Louvet, F. 2018, ARA&A, 56, 41

Myers, P. C. 2009, ApJ, 700, 1609

Nakajima, T., Inoue, H., Fujii, Y., Miyazawa, C., Iwashita, H., Sakai, T., Noguchi, T., & Mizuno, A. 2019, PASJ, 71, 17

Nakamura, F., Sugitani, K., Tanaka, T., et al. 2014, ApJL, 791, L23

Olmi, L., Cunningham, M., Elia, D., & Jones, P. 2016, A&A, 594, A58

Padovani, M., Marcowith, A., Sánchez-Monge, Á., Meng, F., & Schilke, P. 2019, A&A, 630, A72

Panagia, N. 1973, AJ, 78, 929

Peretto, N., & Fuller, G. A. 2009, A&A, 505, 405

Peretto, N., Fuller, G. A., Duarte-Cabral, A., et al. 2013, A&A, 555, 112

Rebull, L. M., Guieu, S., Stauffer, J. R., et al. 2011, ApJS, 193, 25

Rigby, A. J., Peretto, N., Adam, R., et al. 2018, A&A, 615, A18

Rybicki, G. B., & Lightman, A. P., 1979, Radiative processes in astrophysics

Simpson, R. J., Povich, M. S., Kendrew, S., et al. 2012, MNRAS, 424, 2442

Schneider, N., Csengeri, T., Hennemann, M., et al. 2012, A&A, 540, L11

Schuller, F., Menten, K. M., Contreras, Y., et al. 2009, A&A, 504, 415

Smith, R. J., Longmore, S., Bonnell, I. 2009, MNRAS, 400, 1775

Tan, J. C., Beltrán, M. T., Caselli, P., et al. 2014, in Protostars and Planets VI, ed. H. Beuther et al. (Tucson, AZ: Univ. Arizona Press), 149

Tigé, J., Motte, F., Russeil, D., et al. 2017, A&A, 602, A77

Treviño-Morales, S. P., Fuente, A., Sánchez-Monge, Á., et al. 2019, A&A, 629, A81

Urquhart, J. S., König, C., Giannetti, A., et al. 2018, MNRAS, 473, 1059

Umemoto, T., Minamidani, T., Kuno, N., et al. 2017 PASJ, 69, 78

Urquhart, J. S., Moore, T. J. T., Schuller, F., et al. 2013, MNRAS, 431, 1752

Vázquez-Semadeni, E, Gómez, G. C., Jappsen, A. K., Ballesteros-Paredes, J., Klessen, R. S. 2009, ApJ, 707, 1023

Vázquez-Semadeni, E, González-Samaniego, A, & Colín, P. 2017, MNRAS, 467, 1313

Walsh, A. J., Burton, M. G., Hyland, A. R., & Robinson, G. 1998, MNRAS, 301, 640

Walsh, A. J., Breen, S. L., Britton, T., et al. 2011, MNRAS, 416, 1764

**Table 2**
Physical parameters of 17 ATLASGAL dust clumps at 870 $\mu$m taken from Urquhart et al. (2018) (see Figure 2h). All the clumps are located at a distance of 5.0 kpc. Table lists ID, Galactic coordinates ($l$, $b$), 870 $\mu$m integrated flux density ($S_{870}$), radial velocity ($V_{lsr}$), clump effective radius ($R_{clump}$), dust temperature ($T_d$), bolometric luminosity ($L_{bol}$), clump mass ($M_{clump}$), $H_2$ column density ($N(H_2)$), and average volume density ($n_{H_2}$). Massive clumps ($> 10^3$ $M_\odot$) are indicated by daggers.

| ID | $l$ (degree) | $b$ (degree) | $S_{870}$ (Jy) | $V_{lsr}$ (km s$^{-1}$) | $R_{clump}$ (pc) | $T_d$ (K) | $L_{bol}$ ($10^3 \times L_\odot$) | $M_{clump}$ ($10^2 \times M_\odot$) | $N(H_2)$ ($10^{21} \times$ cm$^{-2}$) | $n_{H_2}$ ($10^3 \times$ cm$^{-3}$) |
|---|---|---|---|---|---|---|---|---|---|---|
| c1 | 18.763 | -0.462 | 7.98 | 64.8 | 1.4 | 22.7 | 1.8 | 9.1 | 7.9 | 1.1 |
| c2 | 18.774 | -0.459 | 4.22 | 67.5 | 0.9 | 21.2 | 0.9 | 5.2 | 9.4 | 2.3 |
| c3 | 18.798 | -0.494 | 6.45 | 62.3 | 2.4 | 18.8 | 6.8 | 9.6 | 16.2 | 0.2 |
| c4 | 18.824 | -0.467 | 2.65 | 63.0 | 0.6 | 22.7 | 4.1 | 3.0 | 33.0 | 5.3 |
| c5† | 18.823 | -0.486 | 52.57 | 65.2 | 4.8 | 19.0 | 24.4 | 76.9 | 61.1 | 0.2 |
| c6† | 18.843 | -0.502 | 14.86 | 65.2 | 1.8 | 14.2 | 2.1 | 34.6 | 21.5 | 2.2 |
| c7† | 18.854 | -0.532 | 15.09 | 64.0 | 2.8 | 24.1 | 28.2 | 15.7 | 13.2 | 0.2 |
| c8 | 18.863 | -0.481 | 8.60 | 65.4 | 1.7 | 23.5 | 7.0 | 9.2 | 23.9 | 0.7 |
| c9† | 18.876 | -0.489 | 8.20 | 65.5 | 1.5 | 19.3 | 2.4 | 11.7 | 39.6 | 1.2 |
| c10† | 18.886 | -0.509 | 17.78 | 66.2 | 2.9 | 25.0 | 23.9 | 17.6 | 18.1 | 0.2 |
| c11† | 18.888 | -0.474 | 43.05 | 65.8 | 4.7 | 22.7 | 53.8 | 48.8 | 86.5 | 0.2 |
| c12 | 18.898 | -0.499 | 1.99 | 66.2 | 0.6 | 18.3 | 1.0 | 3.1 | 22.9 | 5.5 |
| c13 | 18.898 | -0.509 | 2.71 | 66.3 | 0.6 | 21.6 | 1.8 | 3.3 | 18.2 | 5.8 |
| c14 | 18.971 | -0.404 | 2.91 | 66.9 | 0.6 | 13.7 | 0.1 | 7.2 | 18.2 | 12.7 |
| c15 | 18.948 | -0.456 | 3.13 | 64.4 | 0.6 | 20.1 | 0.3 | 4.2 | 8.7 | 7.5 |
| c16† | 18.844 | -0.376 | 10.51 | 61.0 | 2.5 | 14.9 | 1.3 | 22.6 | 30.1 | 0.5 |
| c17† | 18.859 | -0.416 | 5.94 | 67.8 | 1.8 | 15.3 | 0.4 | 12.2 | 18.6 | 0.8 |

**Table 3**
Physical parameters of six ATLASGAL clumps derived using the NH$_3$ line data (from Wienen et al. 2012). Table contains the ATLASGAL clump ID, NH$_3$ (1,1) line velocity ($V_{lsr}$), NH$_3$ (1,1) line width ($\Delta V$), kinematical temperature ($T_{kin}$), sound speed ($a_s$), thermal velocity dispersion ($\sigma_T$), non-thermal velocity dispersion ($\sigma_{NT}$), Mach number ($M = \sigma_{NT}/a_s$), and ratio of thermal to non-thermal gas pressure ($R_p = a_s^2/\sigma_{NT}^2$) (see Table 2 and also filled hexagons in Figure 2h).

| clump ID | $V_{lsr}$ (km s$^{-1}$) | $\Delta V$ (km s$^{-1}$) | $T_{kin}$ (K) | $a_s$ (km s$^{-1}$) | $\sigma_T$ (km s$^{-1}$) | $\sigma_{NT}$ (km s$^{-1}$) | $M$ ($\sigma_{NT}/a_s$) | $R_p$ ($a_s^2/\sigma_{NT}^2$) |
|---|---|---|---|---|---|---|---|---|
| c4 | 63.0 | 1.80 | 19.91 | 0.26 | 0.10 | 0.76 | 2.91 | 0.12 |
| c5 | 65.2 | 2.06 | 20.81 | 0.27 | 0.10 | 0.87 | 3.26 | 0.09 |
| c8 | 65.4 | 2.87 | 18.83 | 0.25 | 0.09 | 1.22 | 4.79 | 0.04 |
| c9 | 65.5 | 1.90 | 22.39 | 0.28 | 0.10 | 0.80 | 2.89 | 0.12 |
| c10 | 66.2 | 2.28 | 23.57 | 0.28 | 0.11 | 0.96 | 3.39 | 0.09 |
| c11 | 65.8 | 2.85 | 27.99 | 0.31 | 0.12 | 1.20 | 3.90 | 0.07 |

Wang, Y., Bihr, S., Rugel, M., et al. 2018, A&A, 619, 124
Wenger, T. V., Bania, T. M., Balser, D. S., & Anderson, L. D. 2013, ApJ,764, 34
Westerhout, G. 1958, BAN, 14, 215

Wienen, M., Wyrowski, F., Schuller, F., et al. 2012, A&A, 544, 146
Williams, J P., de Geus, E. J., & Blitz, L. 1994, ApJ, 428, 693
Yang, K. et al. 2019, ApJS, 241, 18
Zinnecker, H., & Yorke, H. W. 2007, ARA&A, 45, 481
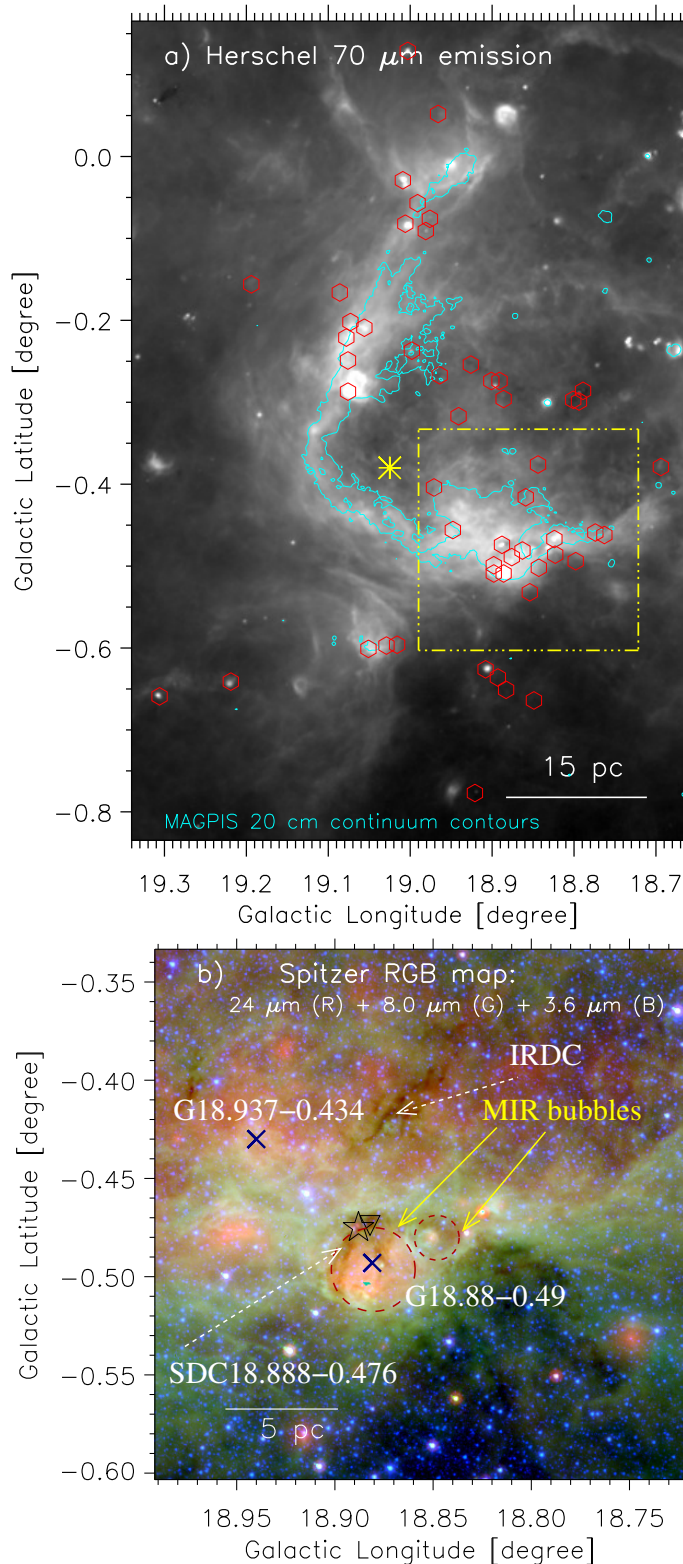
**Figure 1.** a) The panel shows a large-scale view of the complex W39 (selected area $\sim 1°.2 \times 1°.2$ centered at $l = 19°.176$; $b = -0°.333$) using the *Herschel* 70 $\mu$m continuum image. The MAGPIS 20 cm continuum contour (in cyan) is also overplotted with a level of 3.0 mJy beam$^{-1}$. The ATLASGAL dust continuum clumps at 870 $\mu$m (from Urquhart et al. 2018) are also overlaid on the *Herschel* image (see hexagon symbols). An asterisk refers to the position of the exciting star(s) ($l = 19°.025$; $b = -0°.38$), which was previously reported by Kerton et al. (2013) (see also Li et al. 2019). The dotted-dashed box (in yellow) encompasses the area shown in Figure 1b, which is the target area of this paper. The scale bar referring to 15 pc (at a distance of 5.0 kpc) is shown. b) Three color-composite map (*Spitzer* 24 $\mu$m (red), 8.0 $\mu$m (green), and 3.6 $\mu$m (blue) images in log scale) of an area ($\sim 0°.27 \times 0°.27$ centered at $l = 18°.857$; $b = -0°.469$) containing the H II regions G18.88−0.49 and G18.937−0.434. The position of the H II region G18.937−0.434 is obtained from Anderson et al. (2011), while the position of the H II region G18.88−0.49 is taken from Lockman (1989) (see blue crosses). The scale bar referring to 5 pc (at a distance of 5.0 kpc) is shown. Dashed arrows show the locations of the IRDCs, while solid arrows and dashed circles highlight two MIR bubbles. The positions of a water maser and a 6.7 GHz methanol maser are marked by an upside down triangle and a star, respectively.
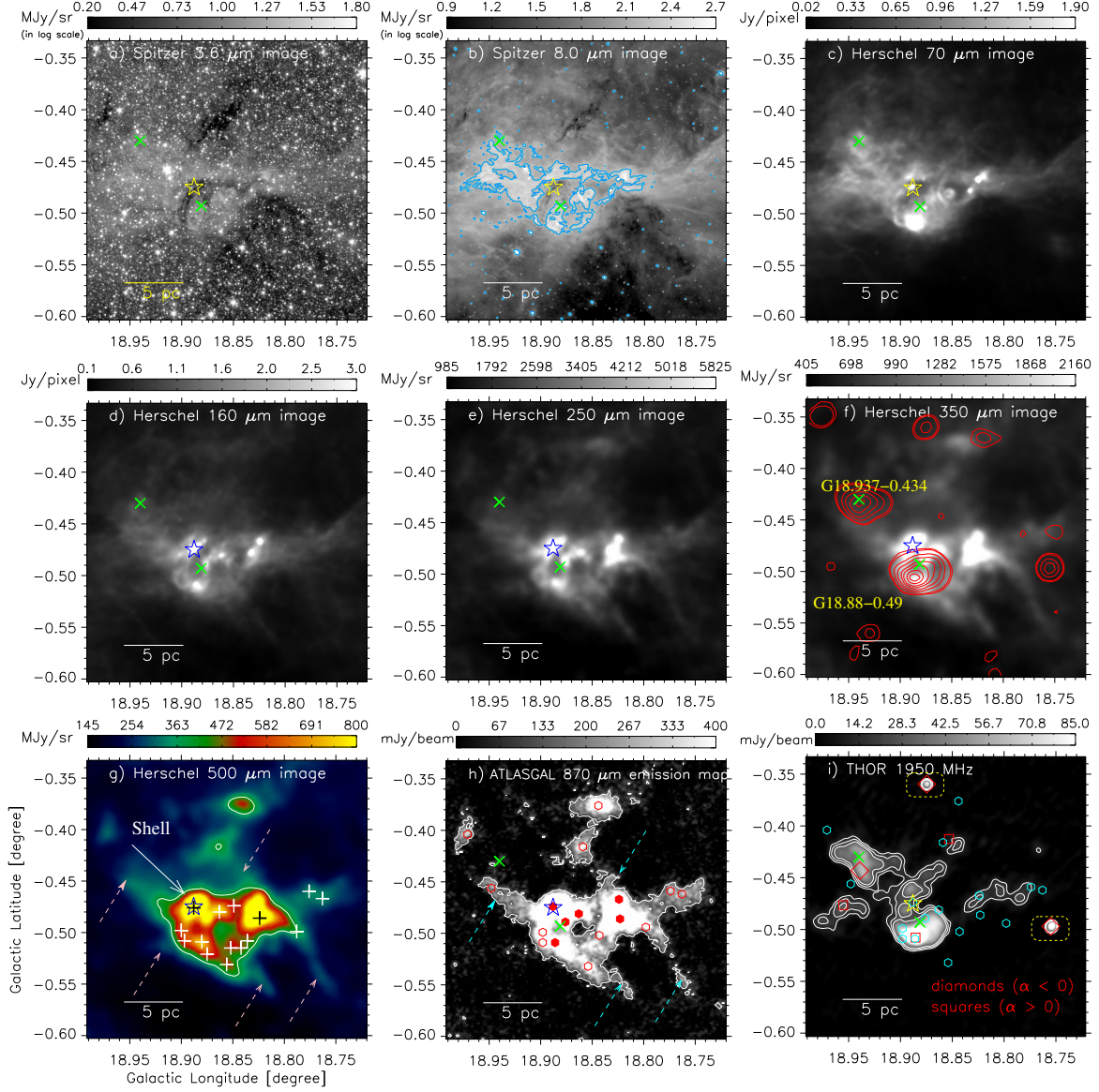
**Figure 2.** Multi-wavelength view of the H II region G18.88−0.49. The images are displayed at different wavelengths, which are highlighted in the panels. Crosses indicate the position of the same H II regions as in Figure 1b, whereas a star represents the position of a 6.7 GHz methanol maser. In panel "b", the *Spitzer* 8.0 μm continuum contour is shown with a level of 230 MJy sr$^{-1}$. In panel "f", the NVSS 1.4 GHz continuum contours (in red) are shown with the levels of 5.45, 8 , 25, 50, 90, 130, 190, and 240 mJy beam$^{-1}$, where 1σ ∼0.45 mJy beam$^{-1}$. In panel "g", the *Herschel* 500 μm continuum contour (in white) indicating a shell-like morphology is shown with a level of 395 MJy sr$^{-1}$, and plus symbols show the positions of NH$_3$ emission reported by Li et al. (2019). In panel "h", the ATLASGAL 870 μm continuum contour (in white) is shown with a level of 125 mJy beam$^{-1}$. The ATLASGAL dust continuum clumps at 870 μm (from Urquhart et al. 2018) are also overlaid on the ATLASGAL image (see empty and filled hexagon symbols and also Figure 1a). Physical parameters derived from the NH$_3$ line data are available for six clumps (filled hexagons; from Wienen et al. 2012). In panels "g" and "h", dashed arrows show potential filaments. In panel "i", the THOR 1950 MHz continuum contours (in white) are shown with the levels of 12, 19, and 28 mJy beam$^{-1}$. In panel "i", open symbols (i.e., squares and diamonds) indicate the radio continuum sources from the THOR survey (Bihr et al. 2016; Wang et al. 2018); squares refer to the sources with spectral index α > 0, and diamonds to sources with α < 0. Two radio clumps appear to be extragalactic objects (see dashed boxes).
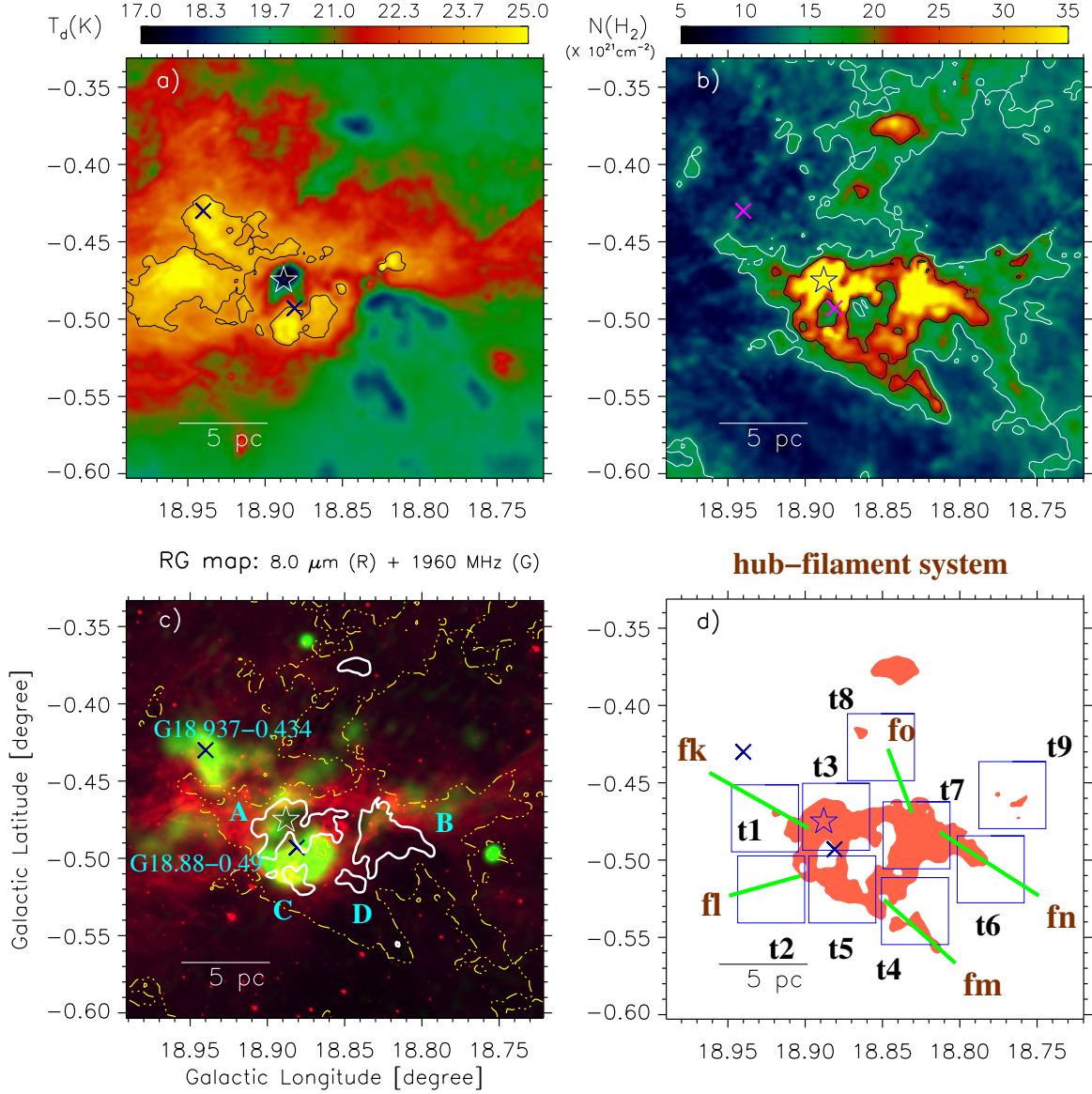
**Figure 3.** a) *Herschel* temperature map. A solid contour (in black) is shown at $T_d = 23.7$ K in the figure. b) *Herschel* column density ($N(H_2)$) map. Filamentary structures are traced in the column density map at a contour level of $14.1 \times 10^{21}$ cm$^{-2}$ (white contour). A solid contour (in black), at $N(H_2) = 21 \times 10^{21}$ cm$^{-2}$, traces a shell-like feature in the figure. c) Overlay of the $N(H_2)$ contours on a two color-composite map (8.0 $\mu$m (red) and 1950 MHz (green) images). A dotted-dashed contour (in yellow) is drawn at $N(H_2) = 14.1 \times 10^{21}$ cm$^{-2}$. A solid white contour at $N(H_2) = 26.4 \times 10^{21}$ cm$^{-2}$ highlights the four subregions, A, B, C, and D. d) The panel shows a hub-filament system around the H II region G18.88−0.49. A filled contour displays the shell-like feature at $N(H_2) = 21 \times 10^{21}$ cm$^{-2}$. A solid contour (in spring green) at $N(H_2) = 26.4 \times 10^{21}$ cm$^{-2}$ shows the four subregions as labeled in Figure 3c. Five filaments seen in the *Herschel* column density map are highlighted by solid lines (fk, fl, fm, fn, and fo), and are also labeled in the figure. Nine small regions (t1 to t9) are also indicated by boxes in the figure, where molecular spectra are extracted (see Figure 4). In each panel, the scale bar, star, and crosses are the same as in Figure 1b.
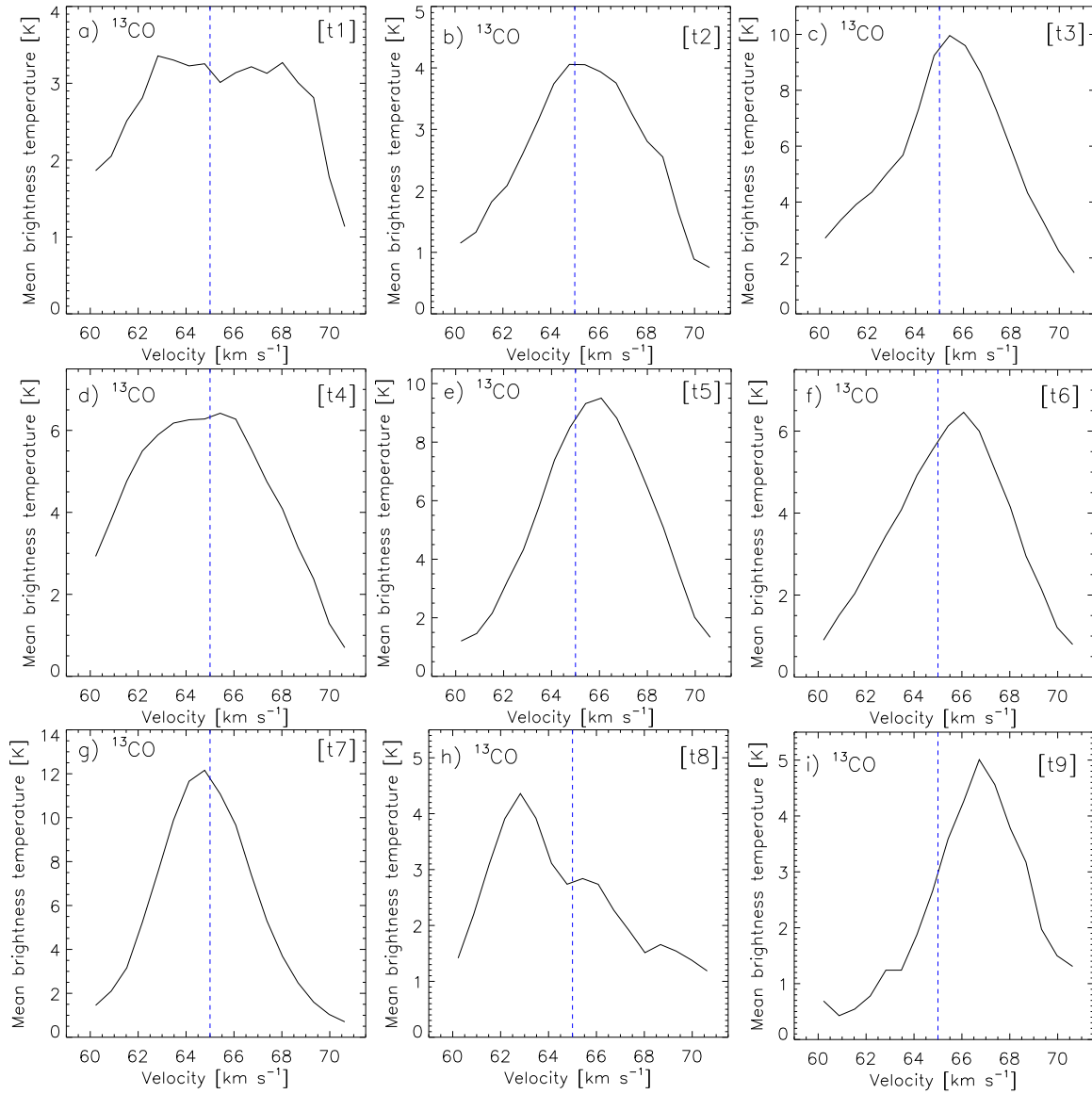
**Figure 4.** $^{13}$CO profiles in the direction of nine small regions (i.e., t1 to t9; see corresponding boxes in Figure 3d). In each panel, a dashed vertical line is drawn at $V_{lsr} = 65$ km s$^{-1}$.
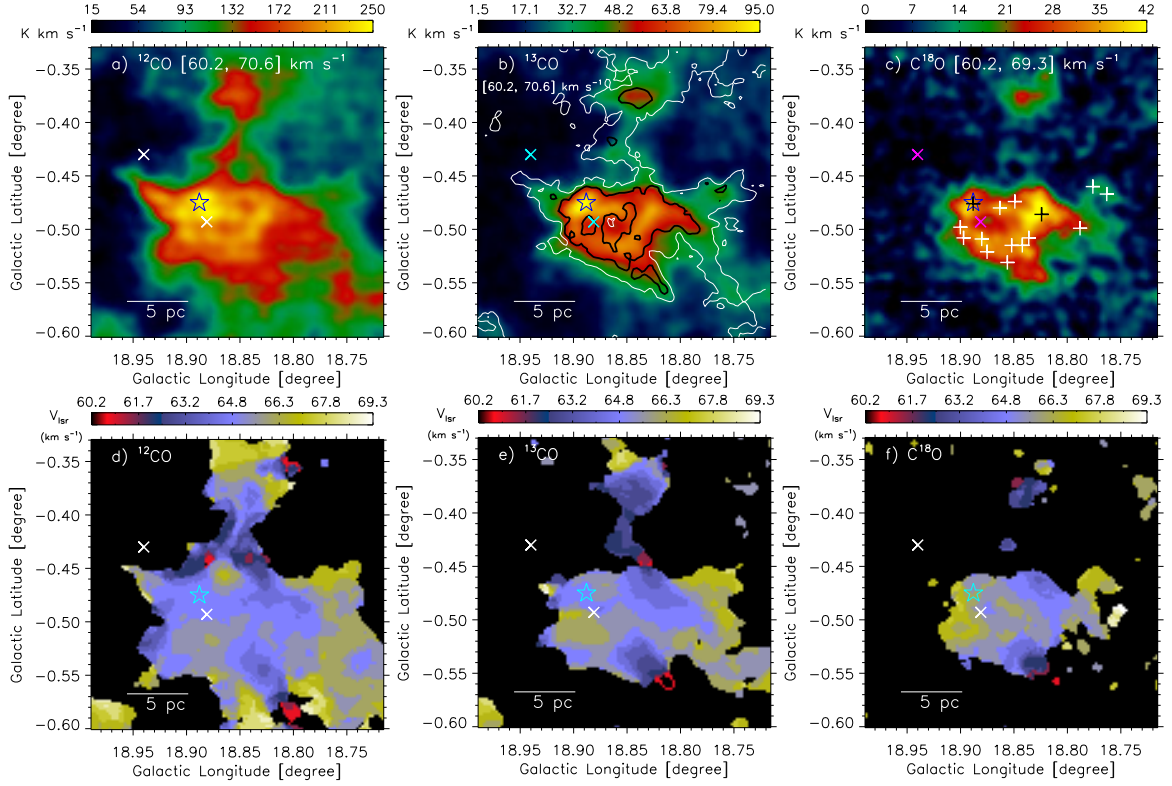
**Figure 5.** FUGIN integrated intensity (or moment-0) maps of a) $^{12}$CO(J =1−0), b) $^{13}$CO(J =1−0), and c) C$^{18}$O(J =1−0) in the direction of the selected area around the H II region G18.88−0.49. FUGIN moment-1 maps of d) $^{12}$CO, e) $^{13}$CO, and f) C$^{18}$O. In panels a), b), and c), the molecular emission is integrated over a velocity interval, which is given in each panel (in km s$^{-1}$). The scale bar, star, and crosses are the same as in Figure 1b. The *Herschel* column density contours are also overlaid on the moment-0 map of $^{13}$CO (see Figure 5b). A thin white contour is shown with the level of $N(H_2) = 14.1 \times 10^{21}$ cm$^{-2}$, while a thick black contour is drawn at the level of $N(H_2) = 21 \times 10^{21}$ cm$^{-2}$. In panel "c", plus symbols highlight the positions of NH$_3$ emission reported by Li et al. (2019).
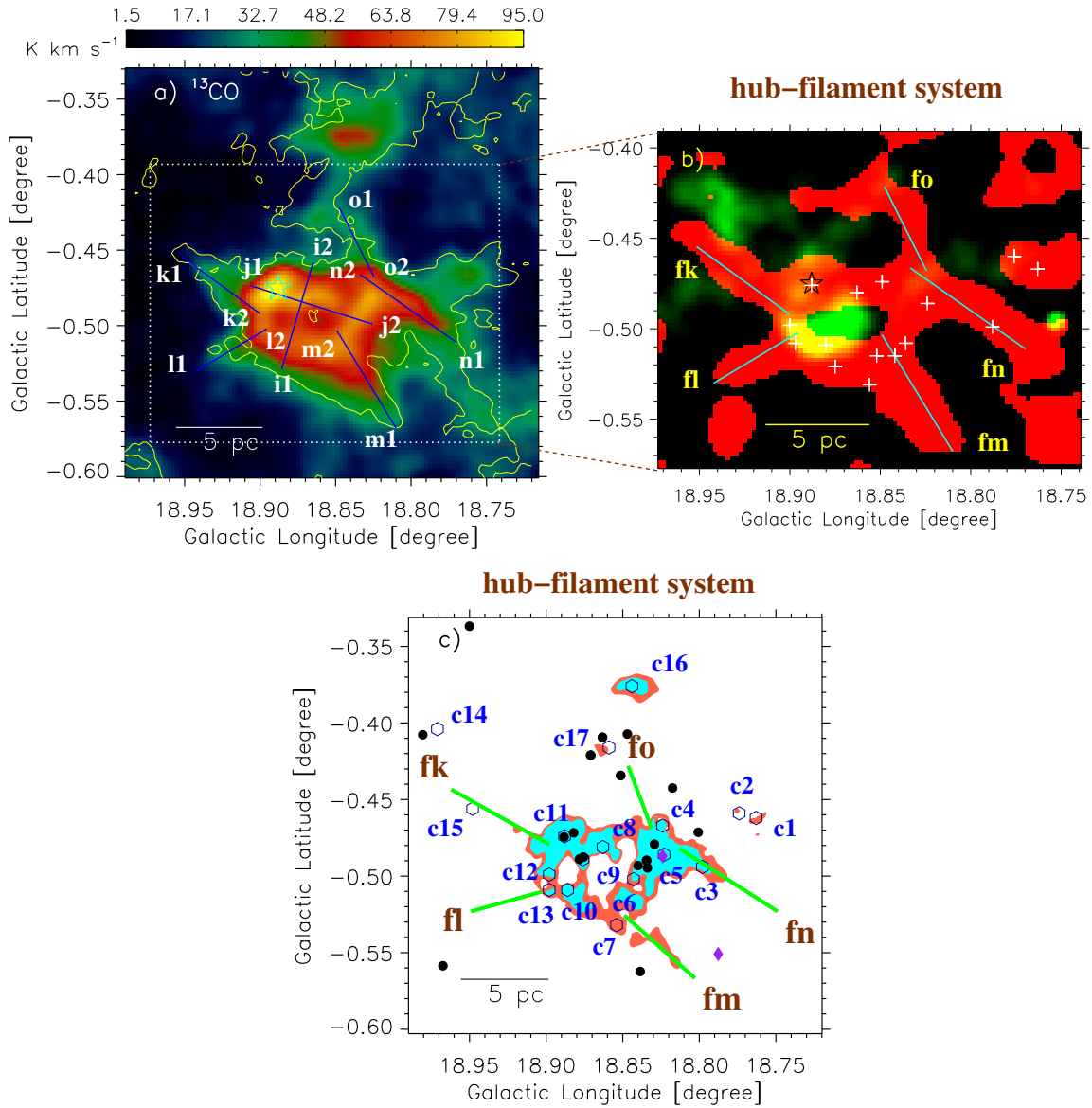
**Figure 6.** a) FUGIN integrated intensity (or moment-0) map of $^{13}$CO (see also Figure 5b). Seven solid lines represent the axes (i.e., "i1–i2", "j1–j2", "k1–k2", "l1–l2", "m1–m2", "n1–n2", and "o1–o2"), where position-velocity diagrams are extracted in Figures 9a– 9g. The dotted box (in white) encompasses the area shown in Figure 6b. b) Overlay of the positions of NH$_3$ emission (see plus symbols; from Li et al. 2019) on a two color-composite map (moment-0 map of $^{13}$CO (red) and 1950 MHz (green) images). The moment-0 map of $^{13}$CO is processed through an "Edge-DoG" algorithm. c) The panel shows a hub-filament system around the H II region G18.88−0.49 as presented in Figure 3d. The panel also displays the positions of Class I YSOs (filled circles), flat-spectrum sources (filled diamonds), and the ATLASGAL clumps (empty hexagons). We identified Class I YSOs and flat-spectrum sources using the *Spitzer* photometric data (see Figure 10 and also text for more details). A shell-like feature is shown by a filled tomato contour at $N(H_2) = 21 \times 10^{21}$ cm$^{-2}$, and a filled cyan contour at $N(H_2) = 26.4 \times 10^{21}$ cm$^{-2}$ highlights four subregions. In each panel, the scale bar is the same as in Figure 1b. In panels "a" and "b", the position of a 6.7 GHz methanol maser is marked by a star.
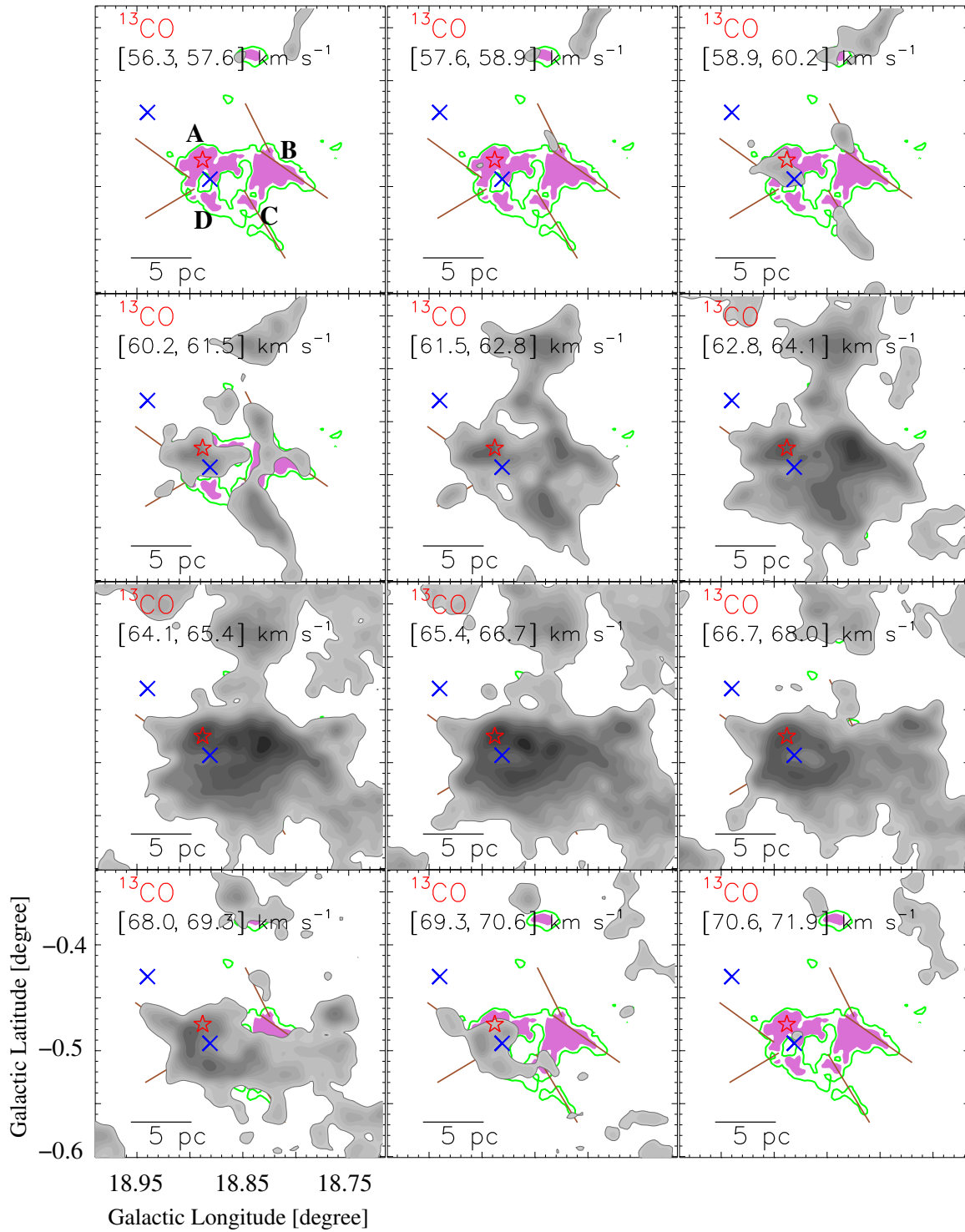
**Figure 7.** Velocity channel maps of the $^{13}$CO emission. The molecular emission is integrated over a velocity interval, which is given in each panel (in km s$^{-1}$). The contour levels are 4.5, 5, 6, 7, 8, 9, 10, 11, 13, 15, 18, 21, 23, 25, and 28 K km s$^{-1}$. In all panels, a shell-like feature is shown by a solid green contour at $N(H_2) = 21 \times 10^{21}$ cm$^{-2}$, and a filled orchid contour at $N(H_2) = 26.4 \times 10^{21}$ cm$^{-2}$ highlights the four subregions, A, B, C, and D. Five solid lines (in brown) represent the locations of the filaments in each panel (see also Figure 3d). In each panel, the scale bar, star, and crosses are the same as in Figure 1b.
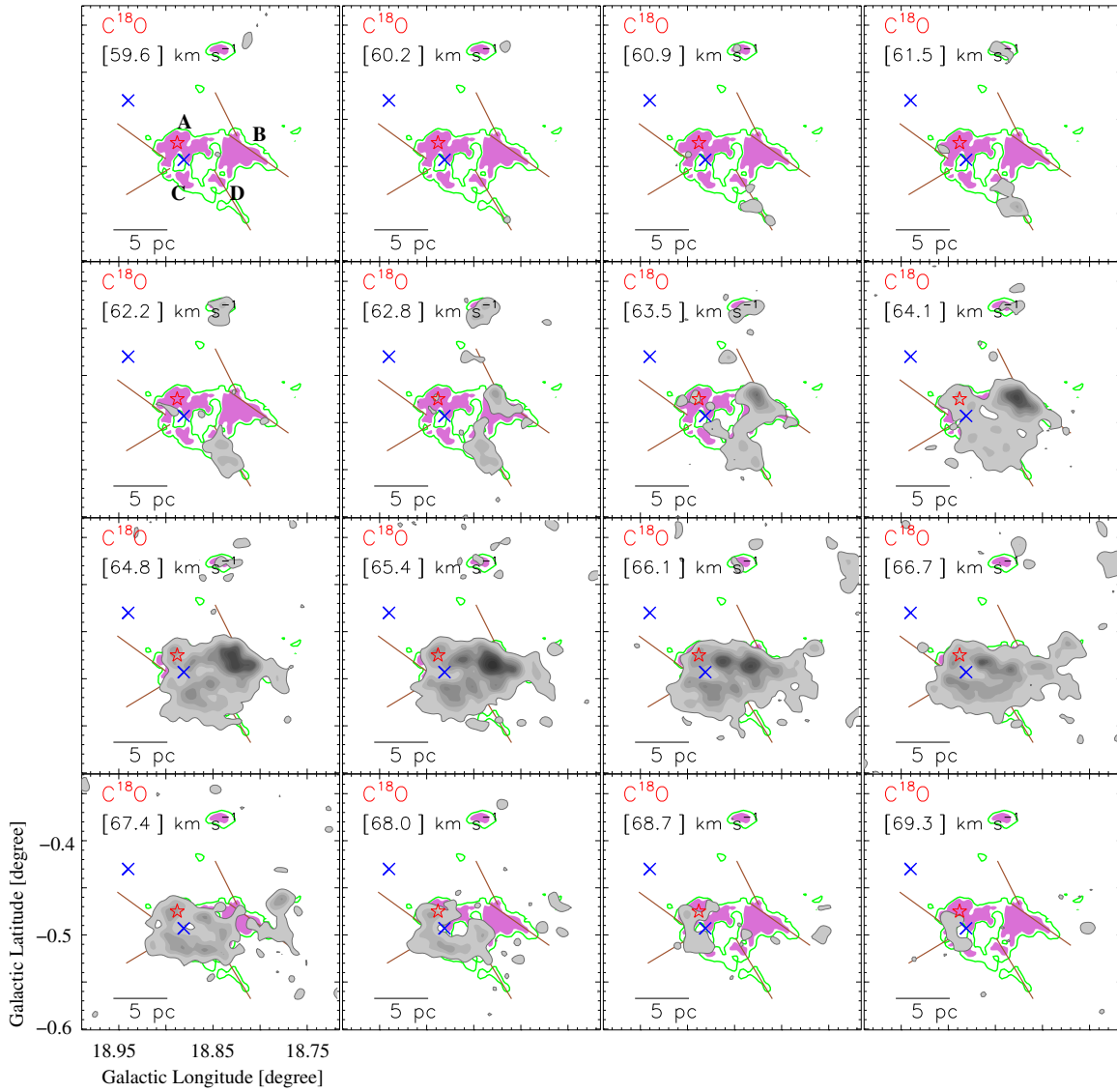
**Figure 8.** Velocity channel maps of the C$^{18}$O emission. The velocity value (in km s$^{-1}$) is labeled in each panel. The contour levels are 1.2, 2, 2.5, 3, 3.5, 3.7, 3.9, 4.1, 4.6, 5, 5.5, 6, and 7.5 K. In all panels, a shell-like feature is shown by a solid green contour at $N(\mathrm{H}_2) = 21 \times 10^{21}$ cm$^{-2}$, and a filled orchid contour at $N(\mathrm{H}_2) = 26.4 \times 10^{21}$ cm$^{-2}$ highlights the four subregions, A, B, C, and D. Five solid lines (in brown) represent the locations of the filaments in each panel (see also Figure 3d). In each panel, the scale bar, star, and crosses are the same as in Figure 1b.
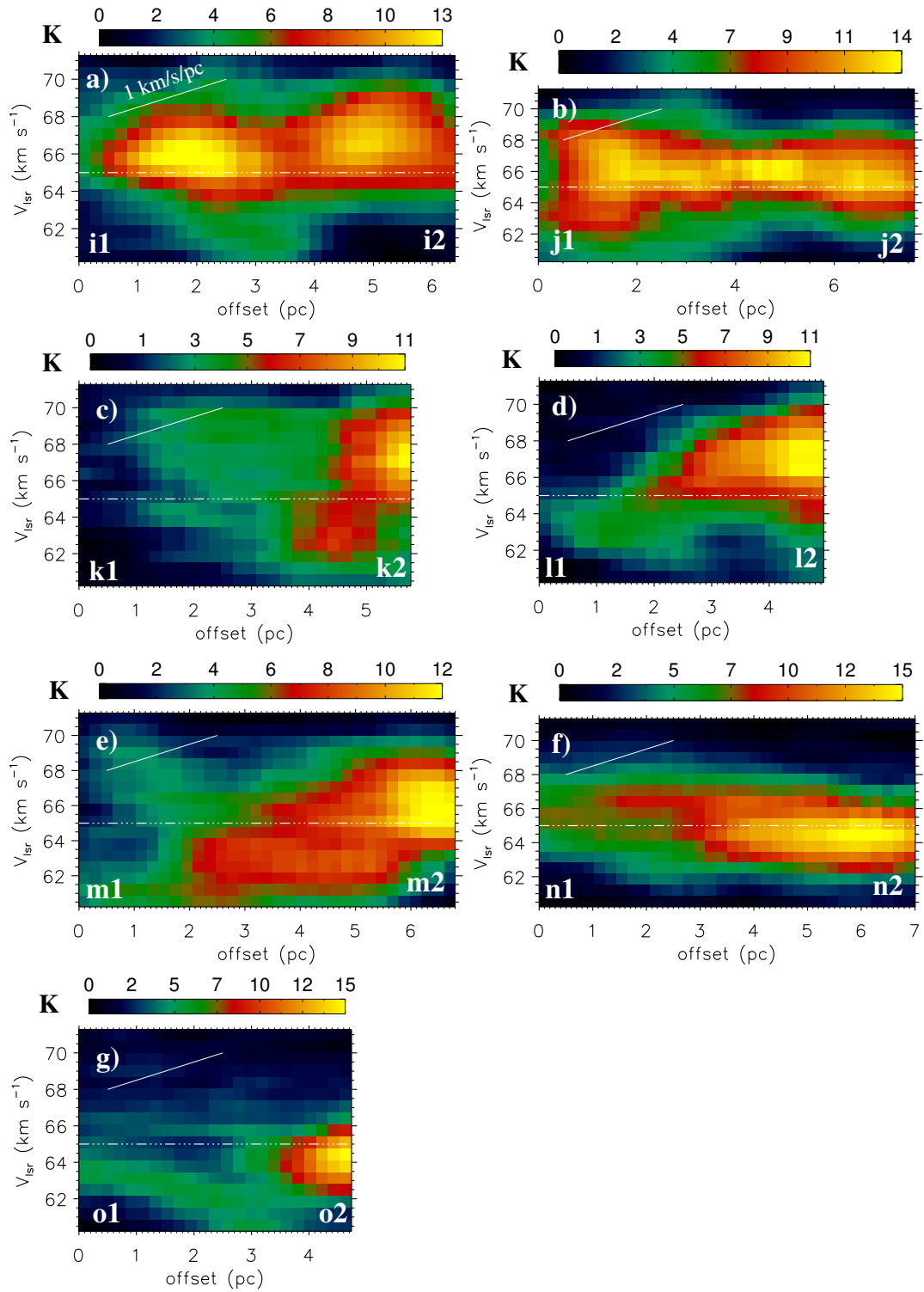
**Figure 9.**  Position-velocity diagrams along the axes a) "i1–i2", b) "j1–j2", c) "k1–k2", d) "l1–l2", e) "m1–m2", f) "n1–n2", and g) "o1–o2" as marked in Figure 6a. In each panel, a horizontal dotted-dashed line is shown at $V_{lsr} = 65$ km s$^{-1}$, and a reference bar at 1 km s$^{-1}$ pc$^{-1}$ is also drawn to facilitate the tracing of velocity gradients.
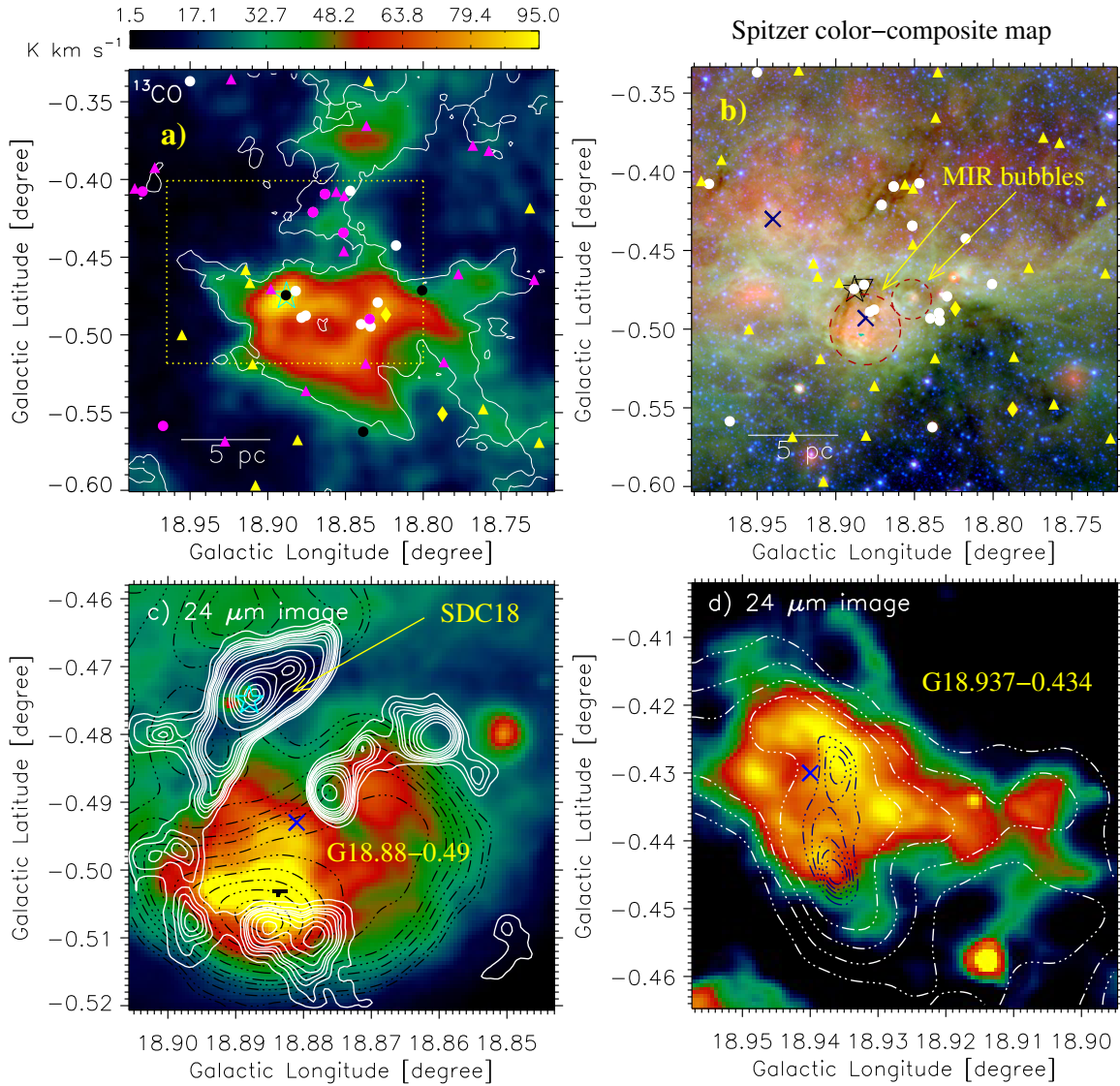
**Figure 10.** a) Overlay of the positions of Class I YSOs (filled circles), flat-spectrum sources (filled diamonds), and Class II YSOs (filled triangles) on the integrated intensity map of $^{13}$CO. The symbols (in black and yellow) refer to the YSOs selected using the color-magnitude plot ([3.6] − [24] vs [3.6]). The YSOs identified using the *Spitzer* color-color plot ([3.6]−[4.5] vs. [5.8]−[8.0]) are highlighted by symbols (in magenta), while the ones in white color are identified using the *Spitzer* color-color plot ([3.6]−[4.5] vs. [4.5]−[5.8]). A dotted yellow box highlights an area, where Kerton et al. (2013) reported the photometric magnitudes of their selected YSOs. The contour and the star symbol are the same as in Figure 6a. b) Overlay of the positions of the selected YSOs (see filled circles, diamonds, triangles and also Figure 10a) on the *Spitzer* color-composite map as shown in Figure 1b. c) A zoomed-in view of an area around the H II region G18.88−0.49 and SDC18 using the *Spitzer* 24 µm image. The map is also overlaid with the IRAM 1.2 mm continuum emission contours from Rigby et al. (2018) (see solid white contours) and the THOR 1950 MHz continuum contours (see dotted-dashed black contours). The contour levels of the IRAM 1.2 mm continuum emission are 28, 38, 45, 50, 55, 65, 75, 85, 100, 150, 220, 260, 300, 370, 500, and 570 mJy beam$^{-1}$, while the contour levels of the THOR continuum emission are (0.08, 0.1, 0.15, 0.2, 0.25, 0.3, 0.4, 0.5, 0.6, 0.7, 0.8, 0.9, 0.95) × 169 mJy beam$^{-1}$. d) A zoomed-in view of an area around the H II region G18.937−0.434 using the *Spitzer* 24 µm image. The map is also overlaid with the THOR 1950 MHz continuum contours (see dotted-dashed navy and white contours). The contour levels of the THOR continuum emission are 12, 22, 32, 42, 55, 58, 60, 61.5, and 63 mJy beam$^{-1}$. In panels, star and crosses are the same as in Figure 1b.